



DIPLOMARBEIT

Micromanipulation and Wave Front Shaping in Disordered Media

ausgeführt am

Institut für Theoretische Physik
der Technischen Universität Wien

Institute for Theoretical Physics
Vienna University of Technology

unter der Anleitung von
Dipl.-Ing. Andre Brandstötter,
Dipl.-Ing. Matthias Kühmayer,
Univ.Prof. Dipl.-Ing. Dr.techn. Stefan Rotter
durch

Michael Horodynski
Grundsteingasse 9/2
A-1160 Wien
michael.horodynski@gmail.com

Datum

Unterschrift

Contents

1. Introduction	1
2. Theoretical Background	3
2.1. Scattering Formalism	3
2.2. The Wigner-Smith Time-Delay Operator and Beyond	5
2.3. Waveguide Physics	7
3. Micromanipulation of a Target	11
3.1. Momentum Transfer onto a Target – Revisited	11
3.1.1. Dielectric Target	12
3.1.2. Metallic Target	15
3.2. Applying Pressure	17
3.2.1. Metallic Target	17
3.2.2. Dielectric Target	19
3.3. Exerting Torque	21
3.3.1. Metallic Target	22
3.3.2. Dielectric Target	23
3.4. Focusing onto a Target	24
4. Discussion	27
4.1. Comparing the GWS-Focus to the Field Matrix Method	27
4.2. Pushing a Target in an Arbitrary Direction	29
4.3. Optical Trapping	31
4.4. Applying Torque without Linear Momentum Transfer	33
4.5. Non-Ideal Conditions	34
5. Summary	37
A. Statistical Tools	39
A.1. Correlation Coefficient	39
A.2. Mean Squared Error	39
Acknowledgments	40
Bibliography	41

Chapter 1.

Introduction

More than 30 years ago Ashkin and his collaborators published a seminal paper in which they introduced optical trapping [1], a technique that allowed them to trap nano-scale dielectric particles immersed in water with a laser beam, i.e., holding the particles in place. This advance laid the foundation of a whole new field in physics, that exploits the transfer of momentum from laser light to mesoscopic objects, allowing to exert forces on these objects [2–4]. Optical trapping is a rich field of research since it is relevant for many important applications like cellular manipulation [5, 6], fluid dynamics [7, 8], micro-robotics [9] and tests of fundamental physics [10, 11].

Light cannot only transfer linear momentum to nanoparticles allowing the construction of an optical trap, but can also be used to transfer angular momentum to a target enabling more advanced micromanipulation schemes. The latter has first been experimentally realized in the 1990s via the absorption of light by nanoparticles [12, 13]. It has also been shown that angular momentum can be transferred to trapped birefringent [14] and asymmetric particles exhibiting shape birefringence [15]. These methods mostly rely on the transfer of spin angular momentum carried by a circularly polarized laser beam. Trapped particles, like microfabricated, asymmetric particles can be rotated via the transfer of orbital and spin angular momentum [16]. One can also take advantage of the intrinsic angular momentum carried by helical beams [17, 18].

What all the above mentioned techniques have in common is that the nanoparticles are immersed in a liquid with uniform refractive index. However, if one wants to trap and manipulate organic structures like biological cells, one has to overcome the hurdle of them being embedded within biological tissue which is a highly turbid and disordered medium due to its spatially non-uniform refractive index. This, in turn, results in optical aberrations [19] and complex scattering processes which distort the wave front such that a Gaussian laser beam which is typically used in optical traps is not the optimal solution for the problem at hand anymore. Therefore, such disordered media pose a great challenge for micromanipulation of particles with light and finding a suitable laser configuration still remains a problem under consideration [20].

Such challenges do not only appear in the field of optical trapping but also in the wave front shaping community. Here one deals with the question of how to optimally engineer a wave front by using spatial light modulators [21] to achieve desired results, like focusing onto a point inside a disordered medium or controlling the propagation through such a medium [22]. Proof-of-principle experiments showed the power of wave front shaping techniques by demonstrating that a disordered material can be used to focus light [23, 24] and to recover images after transmission through highly scattering samples [25].

One of the major challenges in the wave front shaping community is to focus light inside a disordered medium [26]. Especially guidestar based methods are explored in the literature, either using conjugation guidestars [27–37] or feedback guidestars [38–48]. These methods offer a number of interesting applications like the photochemical activation of drugs [49], the photorelease of biomolecules [50], stimulation of neural activity through optogenetic tags [51] and imaging with fluorescent markers [52]. Moreover, focusing techniques can also be used to produce images at higher resolution than before [53].

The implementation of wave front shaping techniques to optical trapping and micromanipulation has only recently started to gain attention [20]. In Ref. [19] the authors achieved trapping for the first time through a highly turbid medium utilizing an iterative complex modulation procedure. Even without the presence of any aberrations caused by turbid media there still exist – to the best of our knowledge – only iterative computational optimization schemes to enhance optical trapping and micromanipulation capabilities [54–57]. These, however, can get stuck in local minima and convergence to the global minimum representing the optimal state cannot be guaranteed.

In this thesis we introduce a protocol that enables the manipulation of particles inside disordered media in many possible ways, such as applying force, pressure or torque, without the need of any optimization schemes. Moreover, we show that our protocol can also be used to achieve optimal focus on such embedded targets.

Chapter 2.

Theoretical Background

As the achievement of the goals listed in the introduction relies heavily on the scattering matrix of the system under consideration, we start by introducing the scattering formalism used throughout this work. We continue by explaining the Wigner-Smith time-delay operator [58, 59] and extend its idea to form the Generalized Wigner-Smith (GWS) operator [60], which serves as the foundation of this work. We conclude this chapter by reviewing the physics of a rectangular waveguide as this is the model system of our choice.

2.1. Scattering Formalism

The primary goal of this section is to introduce the quantity that allows us to connect the incoming flux to the outgoing flux for an arbitrary scattering system [22]. This quantity is the system's scattering matrix S , which allows us to do the bookkeeping of all incoming and outgoing "channels". The states connected by the scattering matrix S are always taken to be in the asymptotic regions of the scattering system, such that all evanescent waves have already decayed.

We consider now the scattering system depicted in Fig. 2.1, which consists of a scattering region bounded by hard walls connected to the outside via two leads, on the left and right, respectively. Such a system has the advantage that all waves either enter or leave through the left or right lead and no radiation is lost (assuming that the scattering potential $V(\mathbf{x})$ does not feature regions with gain and loss). Next, we suppose that we have a complete and orthogonal set of basis states which we will call lead modes in the following, then any given field configuration in the leads is uniquely characterized by the complex expansion coefficients $c_{\gamma,n}^{\pm}$, where n ranges from 1 to N with N being the finite number of flux-carrying lead modes. The coefficients in the left and right lead are denoted by $\gamma = l$ and $\gamma = r$, respectively. The superscripts \pm denote either right-moving (+) or left-moving (−) modes, which can be either ingoing or outgoing depending on the lead. The scattering matrix S now connects all incoming coefficients to all outgoing ones, i.e.,

$$\mathbf{c}_{\text{out}} = S\mathbf{c}_{\text{in}} \quad \text{with} \quad \mathbf{c}_{\text{in}} \equiv \begin{pmatrix} \mathbf{c}_l^+ \\ \mathbf{c}_r^- \end{pmatrix} \quad \text{and} \quad \mathbf{c}_{\text{out}} \equiv \begin{pmatrix} \mathbf{c}_l^- \\ \mathbf{c}_r^+ \end{pmatrix}. \quad (2.1)$$

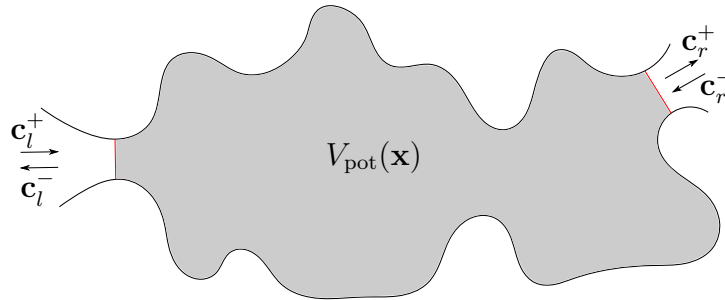


Fig. 2.1. Sketch of a generic scattering geometry bounded by hard walls shown as black lines. The gray-shaded area indicates the scattering region, which is described by a spatially dependent potential $V_{\text{pot}}(\mathbf{x})$. Incoming and outgoing waves pass through the surface areas indicated by red lines and are indicated by their respective expansion coefficients.

The $2N \times 2N$ matrix S can be divided up into four block matrices,

$$S = \begin{pmatrix} r & t' \\ t & r' \end{pmatrix}, \quad (2.2)$$

where the reflection matrix r (r') tells us how an incoming wave from the left (right) lead is reflected back into the left (right) lead and the transmission matrix t (t') contains the transmission amplitudes that characterize the transmission from the left (right) to the right (left).

If the number of modes, N , in the left lead is different from the number of modes, M , in the right lead we can still define a scattering matrix S in Eq. (2.2), with the only difference that r and r' are now matrices of size $N \times N$ and $M \times M$ respectively and t and t' being $M \times N$ and $N \times M$ -dimensional respectively. The total transmission T_n and reflection R_n associated to the incoming flux from the left lead of a certain mode n can be calculated by $T_n = \sum_{m=1}^M |t_{mn}|^2$ and $R_n = \sum_{m=1}^N |r_{mn}|^2$, with equivalent relations for incoming flux from the right. Considering a scattering process without gain and loss, the total transmission and reflection for a given mode must add to 1, i.e., $T_n + R_n = 1$ and $T'_n + R'_n = 1$. If we want to know the total transmission (reflection) of all incoming modes from the left we have to sum over all T_n (R_n), i.e., $T = \sum_{n=1}^N T_n$ ($R = \sum_{n=1}^N R_n$), with similar relations for the incoming flux from the right. The sum of these quantities is given by $T + R = N$ and $T' + R' = M$. We can show that in a system without gain and loss the scattering matrix is unitary, $S^\dagger S = \mathbb{1}$, since the norm of all incoming flux $\sum_n |c_{\text{in},n}|^2 = \mathbf{c}_{\text{in}}^\dagger \mathbf{c}_{\text{in}}$ is equal to the norm of all outgoing flux $\sum_n |c_{\text{out},n}|^2 = \mathbf{c}_{\text{out}}^\dagger \mathbf{c}_{\text{out}}$:

$$\mathbf{c}_{\text{out}}^\dagger \mathbf{c}_{\text{out}} = \mathbf{c}_{\text{in}}^\dagger \mathbf{c}_{\text{in}} \rightarrow \mathbf{c}_{\text{in}}^\dagger (S^\dagger S - \mathbb{1}) \mathbf{c}_{\text{in}} = 0, \quad (2.3)$$

which is only satisfied if $S^\dagger S = \mathbb{1}$. Note that the lead modes need to be flux-normalized for the scattering matrix S to be unitary. If we expand S into the

block-matrix form of Eq. (2.2) the unitary condition gives

$$\begin{aligned} t^\dagger t + r^\dagger r &= t'^\dagger t' + r'^\dagger r' = \mathbb{1}, \\ r^\dagger t' + t^\dagger r' &= t'^\dagger r + r'^\dagger t = 0. \end{aligned} \quad (2.4)$$

The unitarity of S can be reformulated to $SS^\dagger = \mathbb{1}$, which gives

$$\begin{aligned} tt^\dagger + r'r'^\dagger &= t't'^\dagger + rr^\dagger = \mathbb{1}, \\ rt^\dagger + t'r'^\dagger &= tr^\dagger + r't'^\dagger = 0. \end{aligned} \quad (2.5)$$

The scattering matrix S also obeys so-called reciprocity conditions, known as Onsager relations. These relations written out in terms of reflection and transmission matrices are given by $r^T = r$, $r'^T = r'$ and $t^T = t'$, which in short corresponds to a transposition-symmetric scattering matrix $S = S^T$. Loosely speaking, these relations tell us that the scattering process from mode m to mode n happens with the same amplitude as the reverse process. This property is, however, not the same as time-reversal symmetry, because the Onsager relations may still hold in a medium with absorption for which time-reversal symmetry is broken. After introducing the scattering matrix S , we will now use it to construct the Wigner-Smith time-delay operator and generalizations thereof.

2.2. The Wigner-Smith Time-Delay Operator and Beyond

More than 50 years ago Eugene Wigner and Felix Smith introduced an operator in the context of nuclear scattering theory that allows one to measure the time-delay associated with a scattering process [58, 59]. This Wigner-Smith time-delay operator Q is constructed out of a system's scattering matrix S and its derivative with respect to the frequency ω ,

$$Q = -iS^{-1} \frac{dS}{d\omega}. \quad (2.6)$$

It is easy to show that for flux-conserving systems, i.e., for a unitary scattering matrix $S^\dagger S = \mathbb{1}$, the time-delay operator is Hermitian featuring real eigenvalues and a complete and orthogonal set of eigenvectors. The eigenstates \mathbf{u}^i of Q , also known as principal modes, have the feature that the orientation of their output vectors $\mathbf{v}^i = S\mathbf{u}^i$ (in a certain basis) stays invariant under a small change $\Delta\omega$ in the frequency ω ,

$$\left. \frac{d\mathbf{v}^i}{d\omega} \right|_{\omega_0} = i\theta^i \mathbf{v}^i(\omega_0) \rightarrow \mathbf{v}^i(\omega_0 + \Delta\omega) \approx e^{i\theta^i \Delta\omega} \mathbf{v}^i(\omega_0), \quad (2.7)$$

with θ being the eigenvalue of Q , ω_0 the initial frequency and i denotes the i th time-delay eigenvector or eigenvalue [61–66]. In ballistic scattering setups some principal modes feature a particle-like behavior, i.e., their wavefunctions follow classical trajectory-like patterns [61, 65, 66]. The eigenvalues q_n of the time-delay operator Q are the proper delay times of a scattering state, i.e., they measure the duration of the scattering process [59].

Having explained the Wigner-Smith time-delay we now consider the generalized Wigner-Smith (GWS) operator, introduced in Ref. [60], where the authors extend the Wigner-Smith time-delay operator Q in the sense that the derivative of the scattering matrix S is now taken with respect to some arbitrary parameter α which the scattering matrix S depends on, i.e.,

$$Q_\alpha \mathbf{u}_\alpha^i = -iS^{-1} \frac{dS}{d\alpha} \mathbf{u}_\alpha^i = \theta_\alpha^i \mathbf{u}_\alpha^i, \quad (2.8)$$

where α can either be a global parameter, like the position of the whole scattering system [67], or a local parameter, like the position of a single scatterer inside the scattering system [60]. If α is a global parameter the eigenstates of Q_α are invariant with respect to a small parametric shift in α by construction, as can be shown by replacing $\omega \rightarrow \alpha$ in Eq. (2.7). Just like the frequency-derivative in the time-delay operator yields eigenvalues which correspond to the conjugate quantity ω , i.e., the time t , also the GWS-operator Q_α yields eigenvalues which correspond to the conjugate quantity to α . To elucidate this point we give the argument from Ref. [60] here. We start by defining an operator $C_\alpha \equiv -id/d\alpha$, which is the operator corresponding to the conjugate variable of α . The components of C_α in a basis ψ_n are given by

$$[C_\alpha]_{mn} = \left[-i \int_{\partial\Omega} d\xi^D \psi_m^*(x, \xi) \frac{d\psi_n(x, \xi)}{d\alpha} \right]_{x=x_s}, \quad (2.9)$$

where x is the longitudinal coordinate and $\xi = (y, z)^T$ is the transversal coordinate. The integral is performed over a D -dimensional surface $\partial\Omega$ and evaluated at the longitudinal position x_s . Having defined C_α we can use it to construct a “translation” operator $\exp(iC_\alpha\Delta\alpha)$, where $\Delta\alpha$ is the shift in the parameter α . We can use this insight to write the scattering matrix for a shifted parameter $\alpha + \Delta\alpha$ as

$$S(\alpha + \Delta\alpha) = e^{-iC_\alpha\Delta\alpha} S(\alpha) e^{iC_\alpha\Delta\alpha}, \quad (2.10)$$

which can be approximated for small shifts $\Delta\alpha$ by

$$\begin{aligned} S(\alpha + \Delta\alpha) &\approx (\mathbb{1} - iC_\alpha\Delta\alpha) S(\alpha) (\mathbb{1} + iC_\alpha\Delta\alpha) \\ &\approx S(\alpha) - iC_\alpha S(\alpha) \Delta\alpha + iS(\alpha) C_\alpha \Delta\alpha, \end{aligned} \quad (2.11)$$

where we neglect all non-linear terms in $\Delta\alpha$. From this we can construct the derivative of S with respect to α ,

$$\frac{dS}{d\alpha} = \lim_{\Delta\alpha \rightarrow 0} \frac{S(\alpha + \Delta\alpha) - S(\alpha)}{\Delta\alpha} = iS(\alpha)C_\alpha - iC_\alpha S(\alpha), \quad (2.12)$$

which we need to calculate Q_α ,

$$Q_\alpha = -iS^{-1}\frac{dS}{d\alpha} = C_\alpha - S^{-1}C_\alpha S. \quad (2.13)$$

If we now calculate the expectation value of Q_α with respect to some arbitrary input vector \mathbf{c}_{in} we can see that Q_α measures the shift in the conjugated variable to α , if $S^\dagger S = \mathbb{1}$,

$$\mathbf{c}_{\text{in}}^\dagger Q_\alpha \mathbf{c}_{\text{in}} = \mathbf{c}_{\text{in}}^\dagger C_\alpha \mathbf{c}_{\text{in}} - \mathbf{c}_{\text{out}}^\dagger C_\alpha \mathbf{c}_{\text{out}} = \langle C_\alpha \rangle_{\text{in}} - \langle C_\alpha \rangle_{\text{out}}, \quad (2.14)$$

where we again used the input-output relation $\mathbf{c}_{\text{out}} = S\mathbf{c}_{\text{in}}$. This concludes the proof as given in [60] that Q_α measures the shift in the conjugate variable to α between incoming and outgoing waves. Note that this proof is only valid if α is a global parameter. For the case when α is, for example, the longitudinal position x of a single scatterer inside a disordered medium, i.e., α is a local parameter, we can still show numerically in one and two dimensions that the expectation value of Q_x measures the shift in the conjugate variable to x . This conjugate quantity is, however, now the longitudinal momentum shift between incoming and outgoing waves in the vicinity of the single scatterer [60]. This implies that the momentum difference is then transferred onto this target scatterer, providing us with a tool to push a target around, as will be discussed later in detail.

2.3. Waveguide Physics

In this section we review the physics of a semi-infinite rectangular waveguide as depicted in Fig. 2.2a, closely following Refs. [22, 68]. We then show under which circumstances this three-dimensional geometry can be described by a scalar wave equation, the Helmholtz equation, and review its properties.

We start by giving the full solution of Maxwell's equations for a transverse electric field in an empty waveguide in three dimensions, which is

$$\begin{aligned} E_x(t, \mathbf{r}) &= 0, \\ E_y(t, \mathbf{r}) &= -A_y \cos\left(\frac{m\pi y}{W}\right) \sin\left(\frac{n\pi z}{H}\right) e^{i(k_x x - \omega t)}, \\ E_z(t, \mathbf{r}) &= A_z \sin\left(\frac{m\pi y}{W}\right) \cos\left(\frac{n\pi z}{H}\right) e^{i(k_x x - \omega t)}, \end{aligned} \quad (2.15)$$

where $m, n \in \mathbb{N}$, the longitudinal wavenumber is $k_x^2 = \omega^2/c^2 - (m\pi/W)^2 - (n\pi/H)^2$ and the amplitudes A_y and A_z contain all constant prefactors. They are not independent of each other but are related by

$$HmA_y = WnA_z. \quad (2.16)$$

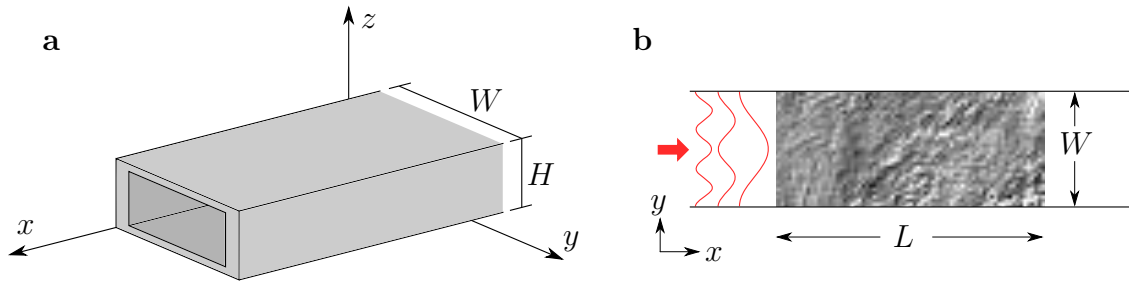


Fig. 2.2. **a**, Sketch of an infinite rectangular empty waveguide with hard walls of height H and width W . **b**, Depiction of a generic scattering system, consisting of a scattering region (textured region) with length L and width W . It is embedded inside a two-dimensional waveguide with hard walls at $y = 0$ and $y = L$ attached to semi-infinite leads on the left and right of the scattering region. The red lines depict the intensity of the first three waveguide modes at a well-defined value of x .

The magnetic field is now simply given by one of Maxwell's equations,

$$\nabla \times \mathbf{E} = -\frac{1}{c} \partial_t \mathbf{B}, \quad (2.17)$$

where we plug in the expression for the electric field given in Eq. (2.15). When split up into its three components, the magnetic field reads

$$\begin{aligned} B_x(t, \mathbf{r}) &= -i \frac{c}{\omega} \left[\frac{m\pi}{W} \hat{E}_z + \frac{n\pi}{H} \hat{E}_y \right] \cos\left(\frac{m\pi y}{W}\right) \cos\left(\frac{n\pi z}{H}\right) e^{i(k_x x - \omega t)}, \\ B_y(t, \mathbf{r}) &= -\frac{ck_x}{\omega} \hat{E}_z \sin\left(\frac{m\pi y}{W}\right) \cos\left(\frac{n\pi z}{H}\right) e^{i(k_x x - \omega t)}, \\ B_z(t, \mathbf{r}) &= -\frac{ck_x}{\omega} \hat{E}_y \cos\left(\frac{m\pi y}{W}\right) \sin\left(\frac{n\pi z}{H}\right) e^{i(k_x x - \omega t)}. \end{aligned} \quad (2.18)$$

If we consider a waveguide whose height H (in z -direction) is small compared to its width W (in y -direction) such that there is no z -dependence in the fields or equivalently that the eigenmodes in the z -direction are not excited, i.e., $n = 0$, Eq. (2.15) tells us that $\hat{E}_y = 0$ and therefore we are only left with $E_z(t, \mathbf{r})$. Assuming a monochromatic electric field, which features a harmonic time dependence, $E_z(t, \mathbf{r}) = \psi(\mathbf{r})e^{-i\omega t}$, the spatially varying part of the electric field can be described by the stationary scalar Helmholtz equation for locally homogeneous media:

$$[\Delta + k^2 n^2(\mathbf{r})] \psi(\mathbf{r}) = 0, \quad (2.19)$$

where Δ is the Laplacian in two dimensions, $k = |\mathbf{k}| = \omega/c$ the wavenumber, $n(\mathbf{r})$ the spatially varying refractive index and $\mathbf{r} = (x, y)^T$. This scalar Helmholtz equation is the wave equation we solve in chapters 3 and 4 to describe the scattering problems considered. Another feature of the Helmholtz equation is the close relation

to the Schrödinger equation that can be seen if we define $E_{\text{light}} = (\hbar\omega)^2/(2mc^2)$ and $V_{\text{light}} = E_{\text{light}}[1 - n^2(\mathbf{r})]$ leading to

$$\left\{ \Delta - \frac{2m}{\hbar^2} [V_{\text{light}}(\mathbf{r}) - E_{\text{light}}] \right\} \psi(\mathbf{r}) = 0. \quad (2.20)$$

This has the consequence that the results we derive in the following chapters are not only valid for electromagnetic radiation, but also for matter waves described by the Schrödinger equation, e.g., electrons. However, there are still fundamental differences in the scattering of light and electrons. First, there are different dispersion relations for light waves ($E \propto p$) and matter waves ($E \propto p^2$). This has the consequence that the temporal dynamics of light and matter waves are very different. Second, for free space propagation the group and phase velocity, $v_g = v_\phi = c$ for light waves are the same resulting in the fact that wave packets preserve their shape. This is not the case for matter waves whose group velocity, $v_g = \hbar k/m$, is different from their phase velocity, $v_\phi = \hbar k/(2m)$, resulting in a spreading of wave packets in free space. Third, since $n(\mathbf{r}) \geq 1$ implies that the light energy is always larger than the light potential, $V_{\text{light}} < E_{\text{light}}$, there can never be a tunneling barrier in a dielectric medium.

Suppose now that we have a two-dimensional waveguide geometry as depicted in Fig. 2.2b, with a scattering region bounded on two sides by hard walls and attached to semi-infinite leads on the left and right. Then (2.19) tells us that the most general solution in the asymptotic region far away from the scattering region either on the left ($\gamma = l$) or on the right ($\gamma = r$) is given by a superposition of right-moving (+) and left-moving (-) modes,

$$\psi(\mathbf{x}) = \sum_{n=1}^N \left[c_{\gamma,n}^+ \chi_n(y) \frac{e^{ik_n^x x}}{\sqrt{k_n^x}} + c_{\gamma,n}^- \chi_n(y) \frac{e^{-ik_n^x x}}{\sqrt{k_n^x}} \right], \quad (2.21)$$

where the transverse mode profiles are given by $\chi_n(y) = \sqrt{2/W} \sin(n\pi y/W)$. The sum is taken over all flux-carrying modes (evanescent modes have died out in the asymptotic region), whose number is N , which is fixed such that the wavenumber in x -direction,

$$k_n^x = \sqrt{\omega^2/c^2 - (n\pi/W)^2}, \quad (2.22)$$

has to be real. This means that the number of modes is given by $N = \lfloor \omega W/(c\pi) \rfloor$, where $\lfloor \dots \rfloor$ denotes the floor operation.

Suppose now that we know the wavefunction $\psi(\mathbf{r}, \mathbf{e}_n^{l,r})$ at every point in space for a generic waveguide geometry as depicted in Fig. 2.2b. The wavefunction was calculated for an injection from the left (right) lead with a modal input coefficient vector \mathbf{e}_n^l (\mathbf{e}_n^r) of size N , which is zero everywhere except for a one at the n -th position. This corresponds to an injection with exactly one transverse mode, either from the left or right. In order to calculate the scattering matrix S in mode basis

with this information, we have to perform overlap integrals of $\psi(\mathbf{r}, \mathbf{e}_n^{l,r})$ with the waveguide modes $\chi_n(y)$. The transmission and reflection amplitudes for injection from the left are given by [69]

$$t_{mn} = \sqrt{k_m^x/k_n^x} \int_0^W \chi_m(y) \psi(x=L, \mathbf{e}_n^l) dy, \quad (2.23)$$

$$r_{mn} = \sqrt{k_m^x/k_n^x} \int_0^W \chi_m(y) \psi(x=0, \mathbf{e}_n^l) - \delta_{mn} dy, \quad (2.24)$$

where the prefactor $\sqrt{k_m^x/k_n^x}$ are flux normalization terms needed to ensure that the scattering matrix is unitary [70]. One important detail is that the solution $\psi(\mathbf{r}, \mathbf{e}_n^{l,r})$ has to be calculated without the flux normalization factors in Eq. (2.21). Thus, the flux normalization terms have to be added manually for the calculation of t and r . In analogy to Eqs. (2.23) and (2.24), the transmission and reflection amplitudes for an input from the right read

$$t'_{mn} = \sqrt{k_m^x/k_n^x} \int_0^W \chi_m(y) \psi(x=0, \mathbf{e}_n^r) dy, \quad (2.25)$$

$$r'_{mn} = \sqrt{k_m^x/k_n^x} \int_0^W \chi_m(y) \psi(x=L, \mathbf{e}_n^r) - \delta_{mn} dy. \quad (2.26)$$

Equipped with these tools we will show in the following how we can use the GWS-operator to micromanipulate a target inside a disordered medium.

Chapter 3.

Micromanipulation of a Target

In this section we introduce new methods for manipulating a target embedded inside a disordered medium based on the GWS-operator $Q_\alpha = -iS^{-1}dS/d\alpha$. First, controlling the momentum transferred onto such a target and thus pushing it in a certain direction was already investigated in [60]. Here we will give a new interpretation of this situation. Next, we utilize the radius R , the rotation angle φ and the refractive index n of a single scatterer to apply pressure, exert a torque or focus onto it, thus introducing new protocols to micromanipulate a target. Throughout this chapter, we assume that we have access to the full scattering matrix S of the system, however, a more realistic case where only a subpart of the scattering matrix is known will be covered in section 4.5.

Our investigations are carried out in two-dimensional waveguide systems which are filled with randomly distributed dielectric scatterers made out of Teflon, where either dielectric or metallic squares or circles of various sizes serve as target scatterers (see Fig. 3.1). We, however, want to stress that our protocols are universally applicable (not only to waveguide systems) as they only rely on the scattering matrix S of the system and its derivation with respect to some arbitrary parameter.

3.1. Momentum Transfer onto a Target – Revisited

The eigenvalues of Q_x , that is the GWS-operator constructed when we use the position of a single target scatterer as our parameter α , can be interpreted as the momentum difference between incoming and outgoing waves in direction of the position shift, $\theta_x = \Delta k$ [60]. The authors showed this by considering the momentum difference between the incoming and outgoing wave,

$$\Delta k = \mathbf{u}^\dagger Q_x \mathbf{u} = \mathbf{u}^\dagger k_{\text{in}} \mathbf{u} - \mathbf{v}^\dagger k_{\text{out}} \mathbf{v} = \theta_x, \quad (3.1)$$

where $\mathbf{v} = S\mathbf{u}$ and the last equality holds if \mathbf{u} is an eigenvector of Q_x . As we already elucidated in section 2.2, conservation of momentum then implies that this momentum difference between the incoming and outgoing wave is transferred onto the target scatterer, enabling us to push it around.

In this section we want to show that the eigenvalues of Q_x cannot only be brought

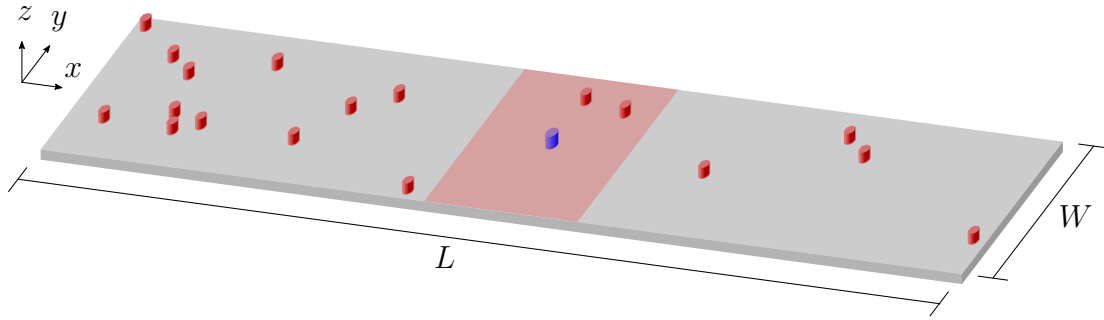


Fig. 3.1. Graphical representation of the waveguide geometry used in the numerical simulations. Depicted is a two-dimensional waveguide geometry with hard walls on the long edges ($L = 6W$) attached to semi-infinite leads on the short edges. The red cylinders indicate the position of randomly distributed Teflon scatterers with a refractive index of $n = 1.44$ and radius $R = 0.0255W$. The blue cylinder tells us the position of the target scatterer, which is of varying size, material and shape depending on the problem. The red-shaded area indicates the region shown in all plots throughout this thesis that depict a spatial intensity distribution.

into a relation with Δk but also with a local quantity constructed out of the intensity at or close to the target's boundary.

3.1.1. Dielectric Target

To motivate the quantity with which we will associate the eigenvalues θ_x of Q_x in the presence of a dielectric target, we first study the situation in one dimension. We start with a potential barrier extending from $x = -L$ to $x = L$ of uniform height $n > 1$ (the refractive index in the asymptotic region is $n_0 = 1$). A depiction of this set-up can be found in Fig. 3.2a. We will prove that there exists a strict linear

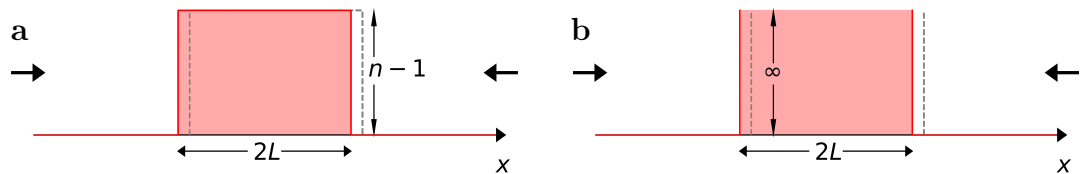


Fig. 3.2. Sketches of the potential barriers (red lines) used for the study of Q_x in one dimension. They have a width of $2L$ and the black arrows indicate that plane waves can be injected from both sides to construct the scattering state. The dashed gray lines show that the barriers are shifted slightly to the right (and left) in order to construct Q_x . **a**, Dielectric potential barrier of height $n - 1$. **b**, Metallic potential barrier of infinite height.

relation between the eigenvalues of Q_x , which is constructed by moving the target slightly to the left and right, and the difference in intensities at the boundaries of the potential barrier. The scattering matrix of such a barrier – calculated by demanding that the wave function and its first derivative are continuous at $x = -L$ and $x = L$ – reads,

$$S_{11} = S_{22} = -\frac{e^{-2ikL} (-1 + e^{4ikLn}) (n^2 - 1)}{e^{4ikLn} (n - 1)^2 - (n + 1)^2}, \quad (3.2)$$

$$S_{12} = S_{21} = -\frac{4e^{2ikL(n-1)}n}{e^{4ikLn}(n - 1)^2 - (n + 1)^2}. \quad (3.3)$$

We then construct Q_x with the help of Eqs. (2.13) and (3.1), where

$$k_{\text{in}} = \begin{pmatrix} k & 0 \\ 0 & -k \end{pmatrix} = -k_{\text{out}}, \quad (3.4)$$

whose matrix elements then read

$$Q_{x,11} = Q_{x,22} = \frac{1}{\Gamma} \left[4k (n^2 - 1)^2 \sin^2 (2kLn) \right], \quad (3.5)$$

$$-Q_{x,12} = Q_{x,21} = \frac{1}{\Gamma} \left[8ikn (n^2 - 1) \sin (2kLn) \right], \quad (3.6)$$

with $\Gamma = -(n^2 - 1)^2 \cos (4kLn) + n^2 (n^2 + 6) + 1 > 0 \quad \forall n, k, L$. The solution of the eigenproblem associated with Q_x is

$$\theta_x^{1,2} = \pm \frac{\sqrt{8}k (n^2 - 1) \sin (2kLn)}{\sqrt{\Gamma}}, \quad (3.7)$$

$$\mathbf{u}_x^{1,2} = \mp \frac{1}{N_{1,2}} \left(\frac{-i}{4n} \left[\sqrt{2\Gamma} \pm 2 (n^2 - 1) \sin (2kLn) \right], 1 \right)^T, \quad (3.8)$$

where $N_{1,2} = |\mathbf{u}_x^{1,2}|$ is the norm of the eigenvectors. We then calculate the difference in intensities at the boundaries of the potential barrier

$$\begin{aligned} F_1 &\equiv |\psi(\mathbf{u}_x^1, x = -L)|^2 - |\psi(\mathbf{u}_x^1, x = +L)|^2 \\ &= -\frac{4\sqrt{2} \sin (2kLn)}{\sqrt{\Gamma}}, \end{aligned} \quad (3.9)$$

$$\begin{aligned} F_2 &\equiv |\psi(\mathbf{u}_x^2, x = -L)|^2 - |\psi(\mathbf{u}_x^2, x = +L)|^2 \\ &= \frac{4\sqrt{2} \sin (2kLn)}{\sqrt{\Gamma}}, \end{aligned} \quad (3.10)$$

where the first argument in the parenthesis tells us which eigenvector of Q_x was used to construct the scattering state. We then compare these two quantities with

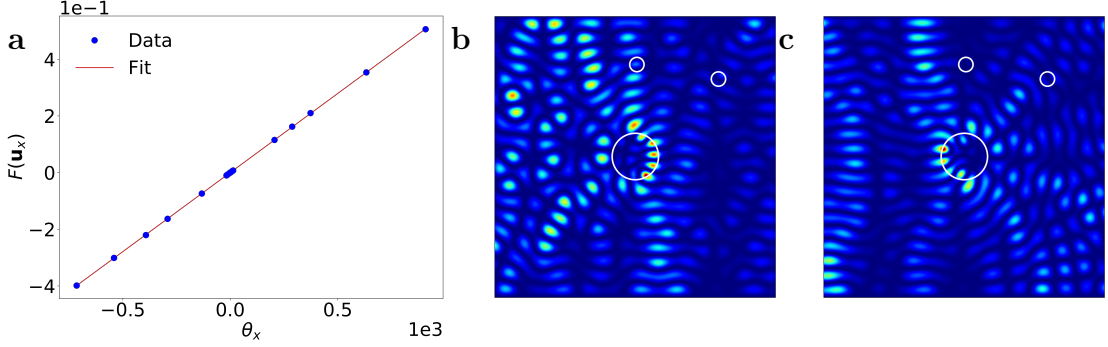


Fig. 3.3. Numerical simulation in the waveguide geometry introduced as in Fig. 3.1 in the presence of a Teflon target (radius $R = 0.0825W$, refractive index $n = 1.44$) with $N = 20$ propagating modes and a wavelength of $\lambda \approx 0.1W$. **a**, Linear relation between the eigenvalues θ_x of the GWS-operator and the quantity F (3.12). The deviation from perfect correlation (see appendix A.1) is only $\Delta r \approx 10^{-5}$. **b**, **c**, Spatial intensity distribution of scattering states constructed by eigenvectors of Q_x corresponding to the largest negative and positive eigenvalues, pushing the target to the left and right, respectively. We show the red-shaded area as depicted in Fig. 3.1 and indicate the position of the scatterers by white circles. The color scale in both plots and all other plots in this thesis has been adjusted to match the maximum intensity in each figure (shown in dark red).

the eigenvalues $\theta_x^{1,2}$ of Q_x and see that

$$\frac{\theta_x^1}{F_1} = \frac{\theta_x^2}{F_2} = -\frac{k(n^2 - 1)}{2}. \quad (3.11)$$

This result concludes the prove that there is a linear relation between the eigenvalues of Q_x and the difference in intensities at the boundaries of the potential barrier. Since we also know that the momentum difference between the incoming and outgoing wave and thus the momentum transfer onto the barrier is equal to the eigenvalues θ_x , we can state that $F_{1,2} \propto \Delta k$. The average force experienced by the target is the momentum transfer per unit time interval. In the stationary case this is the same at all times and thus the momentum transfer is equal to the force. This warrants the naming of the quantity defined above as F . We can use this insight to smoothly tune the momentum transfer onto the potential barrier and also control the directionality of it.

In two dimensions we were not able to provide an analytical expression for Q_x , however, we are still able to show numerically that the radiation force F exerted by the electric field, as given below [55], has an almost perfect correlation to the

eigenvalues of the GWS-operator associated to the shift of a single scatterer:

$$F(\mathbf{u}_{\hat{\mathbf{n}}}^i) \equiv (n^2 - 1) \int_0^{2\pi} \hat{\mathbf{n}} \cdot \begin{pmatrix} \cos \varphi \\ \sin \varphi \end{pmatrix} |\psi(\rho = R)|^2 d\varphi, \quad (3.12)$$

which can be shown (see Fig. 3.3) to be proportional to the eigenvalues of $Q_{\hat{\mathbf{n}}}$, i.e.,

$$F(\mathbf{u}_{\hat{\mathbf{n}}}^i) \propto \theta_{\hat{\mathbf{n}}}^i, \quad (3.13)$$

where the shift of the target scatterer was considered in an arbitrary direction with unit vector $\hat{\mathbf{n}}$. ψ is the electric field distribution of the corresponding eigenstate $\mathbf{u}_{\hat{\mathbf{n}}}^i$ and the integral is performed along the boundary of the circular target with radius R . The spatial intensity distribution of two eigenstates \mathbf{u}_x^i of Q_x , i.e., the GWS-operator for a shift of the scatterer in longitudinal direction x , calculated using an advanced higher-order finite element discretization technique [71, 72] are shown in Fig. 3.3. It is easy to see that there is an intensity build-up on one side of the target, pushing it in positive (right picture) or negative (middle picture) x -direction. In the same figure we also show the almost perfect linear relation, quantified by Pearson's correlation coefficient r (see appendix A.1), between θ_x and the force in direction of the shift F , empirically proving (3.13).

This result allows us to control the transfer of force over several orders of magnitude in an arbitrary direction $\hat{\mathbf{n}}$, thus providing us with a powerful tool for micromanipulation. The only caveat, however, is that the eigenvalues $\theta_{\hat{\mathbf{n}}}^i$ only include information about the momentum transfer in direction of $\hat{\mathbf{n}}$. In general this is accompanied also by a momentum transfer in the direction orthogonal to $\hat{\mathbf{n}}$, which is not controlled by $Q_{\hat{\mathbf{n}}}$, however, a solution to this problem is presented in section 4.2. A considerable advantage of this approach is, that it allows us to construct a scattering state that transfers the optimal amount of momentum onto a target. This is due to the fact that the Hermitian operator $Q_{\hat{\mathbf{n}}}$ has a complete and orthogonal eigenbasis in which every scattering state can be expanded into. This implies that the momentum transfer of an arbitrary scattering state can only be as good as that of the eigenstate associated to the largest eigenvalue. Next, we show how to control the force exerted onto a metallic target.

3.1.2. Metallic Target

As in the preceding section we start the investigation of momentum transfer onto a metallic target with a simple calculation in one dimension. Again, we consider a potential barrier of infinite height extending from $x = -L$ to $x = L$, as is shown in Fig. 3.2b. The scattering matrix for this configuration is

$$S = -e^{-2ikL} \mathbb{1}, \quad (3.14)$$

which agrees with Eqs. (3.2) and (3.3) when we take $\lim_{n \rightarrow \infty} S$. Using Eqs. (2.13) and (3.4) we arrive at

$$Q_x = 2k \begin{pmatrix} 1 & 0 \\ 0 & -1 \end{pmatrix}, \quad (3.15)$$

whose eigenvalues and eigenvectors read

$$\theta_x^1 = 2k, \quad \mathbf{u}_x^1 = (1, 0)^T, \quad (3.16)$$

$$\theta_x^2 = -2k, \quad \mathbf{u}_x^2 = (0, 1)^T. \quad (3.17)$$

Due to the infinitely high barrier, these eigenstates are now given by plane waves which come either from the left or from the right, thus pushing the target in the corresponding direction.

In two dimensions we cannot just use Eq. (3.12) to find a quantity which is proportional to the eigenvalues of $Q_{\hat{\mathbf{n}}}$, since the wavefunction ψ is exactly zero at the boundary. Instead, we calculate F as

$$F(\mathbf{u}_{\hat{\mathbf{n}}}^i) \equiv \int_0^{2\pi} \hat{\mathbf{n}} \cdot \begin{pmatrix} \cos \varphi \\ \sin \varphi \end{pmatrix} |\psi(\rho = R + \epsilon)|^2 d\varphi, \quad (3.18)$$

where ϵ is a small positive real number. The integration path is, compared to a dielectric target, now slightly outside the target's boundary, because the wavefunction at the boundary is exactly zero. This path still gives the correct result because for a small distance outside the target the incidence angle of the waves remains approximately the same. F can once again be shown to be proportional to the eigenvalues of $Q_{\hat{\mathbf{n}}}$, i.e.,

$$F(\mathbf{u}_{\hat{\mathbf{n}}}^i) \propto \theta_{\hat{\mathbf{n}}}^i. \quad (3.19)$$

For $\hat{\mathbf{n}} = (1, 0)^T$ we show in Figs. 3.4b and 3.4c the spatial intensity distribution of eigenstates \mathbf{u}_x associated to large eigenvalues θ_x . One can see that in the middle (right) plot the intensity builds up on the left (right) side, pushing the target to the right (left). Just as in the previous section, we observe an almost perfect linear relation between θ_x and F (see Fig. 3.4a) which empirically confirms our prediction.

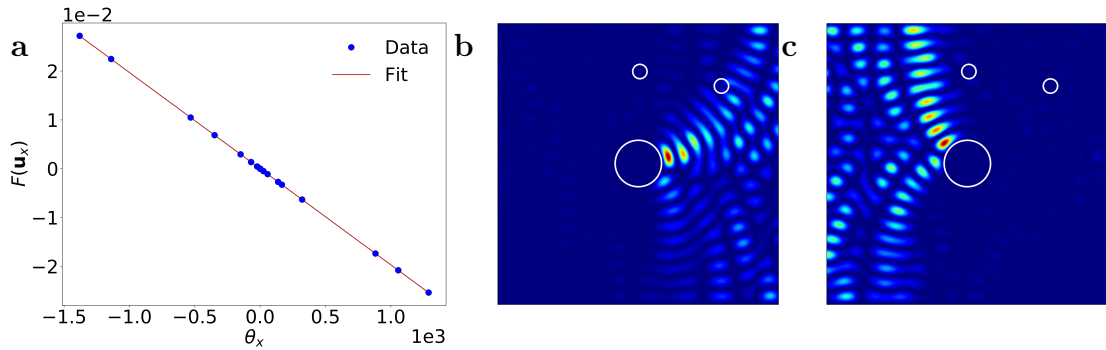


Fig. 3.4. Numerical simulation in the waveguide geometry as introduced in Fig. 3.1 in the presence of a metallic target (radius $R = 0.0825W$) with $N = 20$ propagating modes and a wavelength of $\lambda \approx 0.1W$. **a**, Linear relation between the eigenvalues θ_x of Q_x and the quantity F (3.18). The deviation from perfect correlation is only $\Delta r \approx 10^{-5}$. **b**, **c**, Spatial intensity distribution of scattering states constructed by eigenvectors of Q_x corresponding to the largest negative and positive eigenvalues, pushing the target to left and right, respectively.

3.2. Applying Pressure

After showing how to transfer linear momentum onto a target we move on to the next micromanipulation technique, namely applying pressure onto a target. We achieve this goal by considering the derivative of the scattering matrix S with respect to the radius R of the target, i.e., we construct Q_α with $\alpha = R$. We once again consider a metallic as well as a dielectric target and start by looking at a one-dimensional system to gain first insights. We then expand these insights to two dimensions by considering our two-dimensional waveguide geometry.

3.2.1. Metallic Target

To start the investigation of Q_R , we consider a one-dimensional system in which Q_R turns into Q_L , the GWS-operator we get when taking the derivative of S with respect to L , which is half of the length of the potential barrier. The metallic scatterer is modeled by an infinitely high potential barrier extending from $x = -L$ to $x = L$, as is depicted in Fig. 3.5a. The scattering matrices of this configuration reads:

$$S = -e^{-2ikL} \mathbb{1}, \quad (3.20)$$

The corresponding GWS-Operator, Q_L , then reads

$$Q_L = -iS^{-1} \frac{dS}{dL} = -2k \mathbb{1}. \quad (3.21)$$

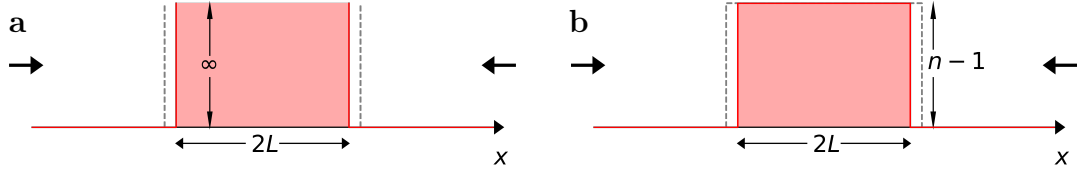


Fig. 3.5. Sketches of the potential barriers (red lines) used for the study of Q_L in one dimension. They have a width of $2L$ and the black arrows indicate that plane waves can be injected from both sides to construct the scattering state. The dashed gray lines show that the barriers are shifted slightly outwards (and inwards) in order to construct Q_R . **a**, Metallic potential barrier of infinite height. **b**, Dielectric potential barrier of height $n - 1$.

If we now take the expectation value of Q_L with an arbitrary unit vector \mathbf{u} , the result is always $\mathbf{u}^\dagger Q_L \mathbf{u} = -2k$. The momentum transfer of a plane wave at wavenumber k that is backreflected at a hard wall is $2k$. This leads us to the conclusion that Q_L measures the sum of the magnitudes of the momentum transferred onto the barrier by arbitrary incoming plane waves from the left and right, which is akin to the radiation pressure.

After getting some intuition for the problem in one dimension we now turn our attention to the two-dimensional problem. Again, an analytical treatment was out of reach for us, but defining in analogy to Eq. (3.18) the following quantity

$$P(\mathbf{u}_R^i) \equiv \int_0^{2\pi} |\psi(\rho = R + \epsilon)|^2 d\varphi, \quad (3.22)$$

it can be shown that

$$P(\mathbf{u}_R^i) \propto \theta_R^i. \quad (3.23)$$

In Fig. 3.6b we show that this linear relation is excellently fulfilled in the simulation, thereby empirically confirming our prediction. We depict the spatial intensity distribution of Q_R -eigenstates corresponding to the largest and smallest eigenvalues in Fig. 3.7. One can see a focus on the boundary of the metal circle for the large eigenvalues and we also see how our eigenstates corresponding to small eigenvalues completely avoid the target. This provides us with a tool that allows us to smoothly vary the pressure applied to the target over many orders of magnitude. Since Q_R has a complete eigenbasis, the maximum amount of pressure we can apply is when we inject the eigenvector corresponding to the eigenvalue with the largest absolute value into the scattering system. Like in the case of $Q_{\hat{\mathbf{n}}}$, we also get an unwanted linear momentum transfer onto the target in the case of Q_R – an issue that will be covered and solved in section 4.3.

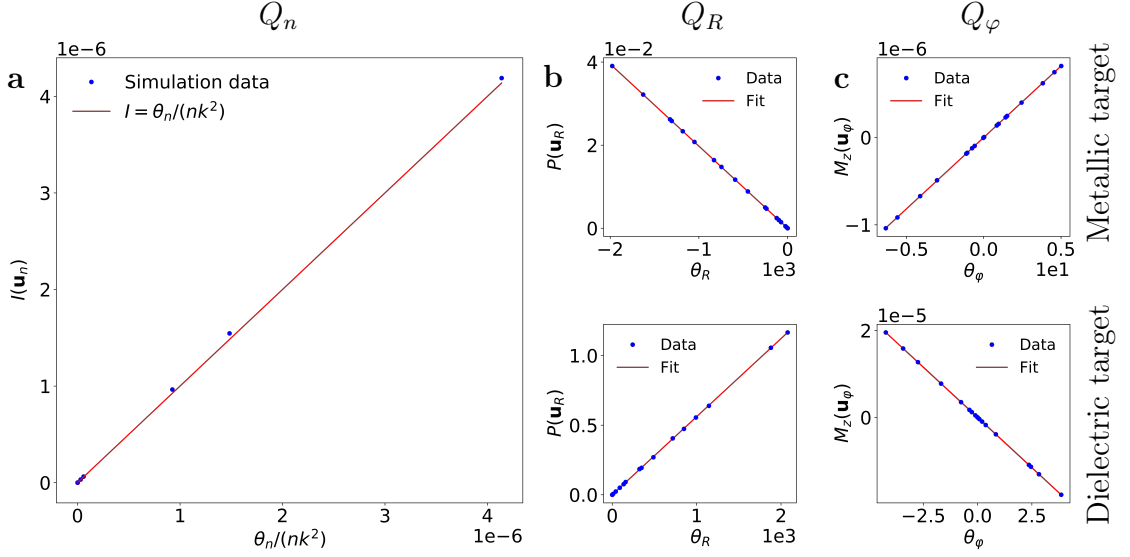


Fig. 3.6. Linear relations of the GWS-eigenvalues with the quantities defined in Eqs. (3.47), (3.22), (3.33), (3.35) and (3.37), for $N = 20$ open modes and a wavelength of $\lambda \approx 0.1W$. **a**, Stored intensity I in a Teflon target ($n = 1.44$) as a function of the eigenvalues θ_n . The deviation from perfect correlation (see appendix A.1) is $\Delta r \approx 10^{-5}$ and the mean squared error with respect to $I = \theta_n/(nk^2)$ is of the order of 10^{-16} . **b**, Upper (lower) plot shows the pressure P as a linear function of the eigenvalues θ_R in the case of a metallic (Teflon) target. For both linear relations the deviation from perfect correlation is $\Delta r \approx 10^{-5}$. **c**, Upper (lower) plot shows the torque M_z as a linear function of the eigenvalues θ_φ in the case of a metallic (Teflon) target. Again, for both linear relations the deviation from perfect correlation is $\Delta r \approx 10^{-6}$.

3.2.2. Dielectric Target

To learn something about Q_R in the presence of a dielectric target we once again consider the potential barrier (shown in Fig. 3.5b) used in 3.1.1. The scattering matrix is then,

$$S_{11} = S_{22} = -\frac{e^{-2ikL}(-1 + e^{4ikLn})(n^2 - 1)}{e^{4ikLn}(n-1)^2 - (n+1)^2}, \quad (3.24)$$

$$S_{12} = S_{21} = -\frac{4e^{2ikL(n-1)}n}{e^{4ikLn}(n-1)^2 - (n+1)^2}. \quad (3.25)$$

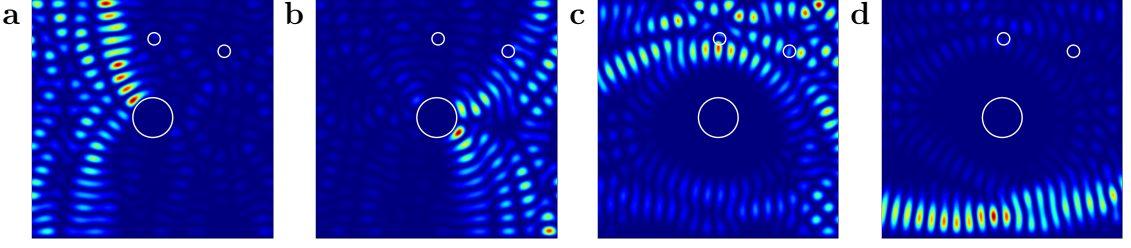


Fig. 3.7. Numerical simulation in the waveguide setup with a metallic target (radius $R = 0.0825W$). The number of propagating modes used is $N = 20$ and the wavelength is $\lambda \approx 0.1W$. **a, b**, Spatial intensity distribution of the two Q_R -eigenstates corresponding to the eigenvalues θ_R with the largest negative value. A strong focusing over a broader area of the target can be observed. **c, d**, Spatial intensity distribution of the two Q_R -eigenstates with the eigenvalues θ_R closest to zero. A strong avoidance of the target scatterer can be clearly observed.

The components of $Q_L = -iS^{-1}dS/dL$ then read

$$Q_{L,11} = Q_{L,22} = -\frac{2k(n^2 - 1)[3n^2 + (n^2 - 1)\cos(4kLn) + 1]}{-(n^2 + 6)n^2 + (n^2 - 1)^2\cos(4kLn) - 1}, \quad (3.26)$$

$$Q_{L,12} = Q_{L,21} = -\frac{8kn^2(n^2 - 1)\cos(2kLn)}{-(n^2 + 6)n^2 + (n^2 - 1)^2\cos(4kLn) - 1}. \quad (3.27)$$

The solution of Q_L 's eigenproblem is

$$\theta_L^1 = \frac{-4k(n^2 - 1)\cos^2(kLn)}{(n^2 - 1)\cos(2kLn) - n^2 - 1}, \quad \mathbf{u}_L^1 = \frac{1}{\sqrt{2}} \begin{pmatrix} 1 \\ 1 \end{pmatrix}, \quad (3.28)$$

$$\theta_L^2 = \frac{4k(n^2 - 1)\sin^2(kLn)}{(n^2 - 1)\cos(2kLn) + n^2 + 1}, \quad \mathbf{u}_L^2 = \frac{1}{\sqrt{2}} \begin{pmatrix} -1 \\ 1 \end{pmatrix}. \quad (3.29)$$

In view of Eq. (3.21), which tells us that the eigenvalues of Q_L are proportional to the pressure applied to the potential barrier, we conjecture that the Q_L -eigenvalues are proportional to the sum of the intensities on the target edges, which are

$$\begin{aligned} P_1 &\equiv |\psi(\mathbf{u}_L^1, x = -L)|^2 + |\psi(\mathbf{u}_L^1, x = L)|^2 \\ &= \frac{-8\cos^2(kLn)}{(n^2 - 1)\cos(2kLn) - n^2 - 1}, \end{aligned} \quad (3.30)$$

$$\begin{aligned} P_2 &\equiv |\psi(\mathbf{u}_L^2, x = -L)|^2 + |\psi(\mathbf{u}_L^2, x = L)|^2 \\ &= \frac{8\sin^2(kLn)}{(n^2 - 1)\cos(2kLn) + n^2 + 1}, \end{aligned} \quad (3.31)$$

where the first argument of the parentheses tells us which eigenvector of Q_L was used to calculate P_i . From those two expressions it's easy to conclude that there is

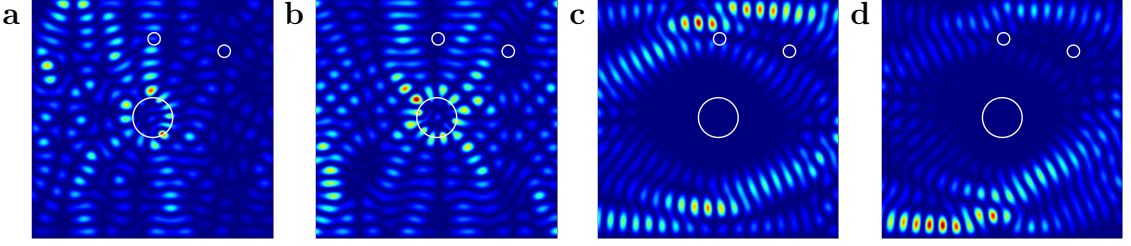


Fig. 3.8. Numerical simulation in the waveguide setup with a Teflon target scatterer (radius $R = 0.0825W$, refractive index $n = 1.44$). The number of propagating modes used is $N = 20$ and the wavelength is $\lambda \approx 0.1W$. **a, b**, Spatial intensity distribution of the two Q_R -eigenstates with the largest eigenvalues θ_R . A strong focusing on the boundary of the target scatterer can be clearly observed. **c, d**, Spatial intensity distribution of the two Q_R -eigenstates with the smallest eigenvalues θ_R . A strong avoidance of the target scatterer can be clearly observed.

a strict linear relation between P_i and θ_L^i ,

$$\frac{\theta_L^1}{P_1} = \frac{\theta_L^2}{P_2} = \frac{k}{2} (n^2 - 1), \quad (3.32)$$

which proves our conjecture.

From these one-dimensional considerations we now generalize this result to two dimensions. Just as for the metallic target, we introduce the quantity

$$P(\mathbf{u}_R^i) \equiv \int_0^{2\pi} |\psi(\rho = R)|^2 d\varphi, \quad (3.33)$$

which can again be shown to be proportional to the Q_R -eigenvalues, i.e.,

$$P(\mathbf{u}_R^i) \propto \theta_R^i. \quad (3.34)$$

We confirm this conjecture by observing an almost perfect linear correlation in our simulations which can be seen in Fig. 3.6b. To further support our argument we show in Fig. 3.8 the spatial intensity distribution of the two eigenstates of Q_R corresponding to the largest eigenvalues and two eigenstates of Q_R corresponding to the smallest eigenvalues. One can clearly observe the focus onto the target's boundary, applying strong pressure and the avoidance of the target, exerting almost no pressure. We also know that the pressure exerted by the eigenstate corresponding to the largest eigenvalue is the theoretical maximum, since Q_R has a complete eigenbasis. This makes our approach particularly attractive.

3.3. Exerting Torque

The third and last technique we present to manipulate a target is to apply torque on it, e.g., with the purpose to rotate the target. We can achieve this goal by

considering the rotation angle φ of the target as the parameter α . Since the rotation of a circle around its center leads, of course, to no changes, we consider a metallic or dielectric square as the target. Because there is no one-dimensional analog to a rotation, we will immediately consider the two-dimensional waveguide depicted in Fig. 3.1.

3.3.1. Metallic Target

In analogy to the quantities we have defined so far, we directly introduce the torque applied to a metallic square target by the electric field. Putting a Cartesian coordinate system right at the center of the square, the torque in its natural definition (" $\mathbf{r} \times \mathbf{F}$ ", with \mathbf{r} the distance to the center and \mathbf{F} the force) is given by

$$M_z(\mathbf{u}_\varphi^i) \equiv \int_{C_1}^{C_2} y |\psi(x = -b_\epsilon, y)|^2 dy + \int_{C_2}^{C_3} x |\psi(x, y = -b_\epsilon)|^2 dx - \int_{C_3}^{C_4} y |\psi(x = b_\epsilon, y)|^2 dy - \int_{C_4}^{C_1} x |\psi(x, y = b_\epsilon)|^2 dx, \quad (3.35)$$

where x and y measure the distance to the center respectively and $|\psi(\mathbf{r})|^2$ gives the radiation force at a certain point in space. We also use $b_\epsilon = L/2 + \epsilon$, where L is the side length of the square and ϵ is a small positive real number. The C_i 's stand for the square's four corners, starting in the upper left corner (C_1), where the addition of ϵ in b_ϵ gives an integration path slightly outside the boundary of the square. Also this expression can be shown to be linear proportional to the eigenvalues of Q_φ , i.e.,

$$M_z(\mathbf{u}_\varphi^i) \propto \theta_\varphi^i, \quad (3.36)$$

which provides us with a technique to smoothly vary the torque applied to the square by choosing superpositions of eigenstates with large or small eigenvalues. Moreover, we can control whether the applied torque rotates the target in a clockwise or counterclockwise direction by considering the sign of the eigenvalues θ_φ . In Fig. 3.6c we empirically confirm the above statement by showing the almost perfect correlation of the eigenvalues θ_φ^i and the torque $M_z^A(\mathbf{u}_\varphi^i)$. To support our argument we show in Fig. 3.9 the spatial intensity distribution of the eigenstates corresponding to the two eigenvalues with the largest absolute value and the two smallest eigenvalues. One can clearly see for the case of large eigenvalues that the intensity builds up on the corners in such a way that torque can be transferred, whereas for the case of small eigenvalues, the wave avoids the scatterer. Following the same arguments as for the other GWS-operators, we conclude that also for Q_φ the eigenstate corresponding to the largest eigenvalue gives us the maximal transferable torque onto the target scatterer. In the next section we show that the transfer of torque is also possible for a dielectric target.

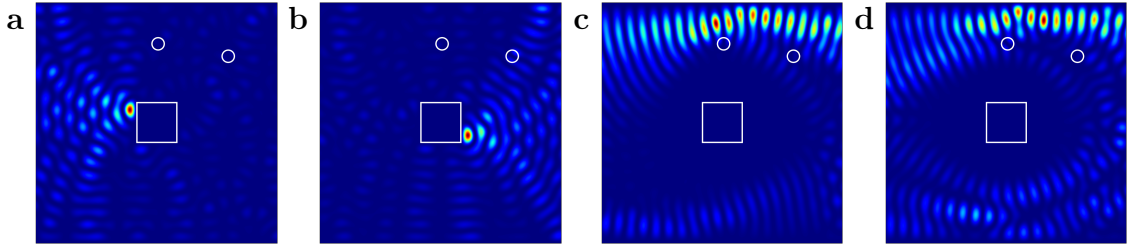


Fig. 3.9. Numerical simulation in the waveguide setup with a metallic square (side length $L = 0.165W$) as the target scatterer. The number of propagating modes used is $N = 20$ and the wavelength is $\lambda \approx 0.1W$. **a, b**, Spatial intensity distribution of the two Q_φ -eigenstates associated to the eigenvalues θ_φ with the largest absolute value. A strong focus onto the corners of the target can be clearly observed leading to a torque. **c, d**, Spatial intensity distribution of the two Q_φ -eigenstates with the smallest eigenvalues θ_φ . A strong avoidance of the target scatterer can clearly be observed.

3.3.2. Dielectric Target

In analogy to section 3.2 we now look at the quantity M_z in the case of a dielectric target

$$M_z(\mathbf{u}_\varphi^i) \equiv \int_{C_1}^{C_2} y |\psi(x = -b, y)|^2 dy + \int_{C_2}^{C_3} x |\psi(x, y = -b)|^2 dx - \int_{C_3}^{C_4} y |\psi(x = b, y)|^2 dy - \int_{C_4}^{C_1} x |\psi(x, y = b)|^2 dx, \quad (3.37)$$

whose definition differs from Eq. (3.35) only by the integration path which now follows the scatterer's boundary, i.e., $b_\epsilon \rightarrow b = L/2$. As expected, one can show that – as in the case of a metallic scatterer – there exists a linear relation, i.e.,

$$M_z(\mathbf{u}_\varphi^i) \propto \theta_\varphi^i, \quad (3.38)$$

which is to be confirmed in the same ways as before by numerical simulations. The result for one such simulation is depicted in Fig. 3.6c. To support our argument we show in Fig. 3.10 the spatial intensity distribution for the eigenstates with the two largest and smallest eigenvalues. For the eigenstates with large eigenvalues one can clearly see that intensity builds up mainly on the square's corners, transferring torque whereas the eigenstates with small eigenvalues once again avoid the target. We also emphasize that, since Q_φ has a complete eigenbasis, the transferred torque we get when constructing the scattering state with the eigenvector associated to the largest eigenvalue is the theoretical maximum. Having shown how to apply a force, pressure or torque onto a target, we will show next a method for focusing onto a target.

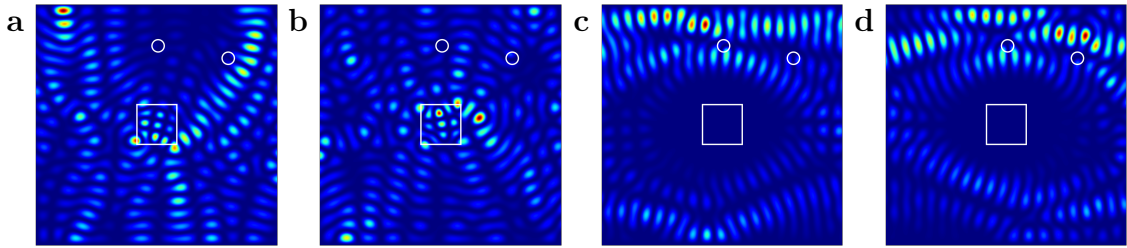


Fig. 3.10. Numerical simulation in the waveguide setup with a Teflon square (side length $L = 0.165W$, refractive index $n = 1.44$) as the target scatterer. The number of propagating modes used is $N = 20$ and the wavelength is $\lambda \approx 0.1W$. **a, b**, Spatial intensity distribution of the two Q_φ -eigenstates corresponding to the eigenvalues θ_φ with the largest absolute value. A strong focusing on the corners of the target scatterer, evidently transferring torque, can be clearly observed. **c, d**, Spatial intensity distribution of the two Q_φ -eigenstates with the smallest eigenvalues $|\theta_\varphi|$, showing a strong avoidance of the target scatterer can be clearly observed.

3.4. Focusing onto a Target

The GWS-operator cannot only be used to manipulate a target, but can also be utilized to focus onto it. We achieve this by considering the derivative of the scattering matrix S with respect to the refractive index n of a dielectric target, i.e., $\alpha = n$. Before we consider focusing in two dimensions we analytically derive in one dimension that there is a strict linear relation between the eigenvalues of Q_n and the degree of focus at a target scatterer. From now on we define focusing as dumping as much intensity as possible into a target area, i.e., maximizing the integrated spatial intensity of the scattering state inside the target.

Our proof considers the same set-up as in Sec. 3.1.1, which is a rectangular potential barrier of height $n > 1$ extending from $x = -L$ to $x = L$ and we show it in Fig. 3.11. To calculate $Q_n = -iS^{-1}dS/dn$, we need the system's scattering

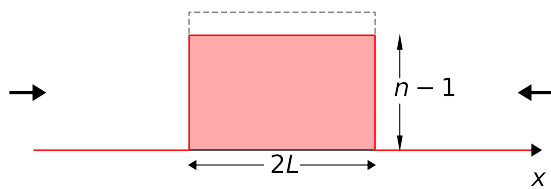


Fig. 3.11. Sketch of the potential barrier (red line) used for the study of Q_n in one dimension. It has a width of $2L$ and a height of $n-1$. The black arrows indicate that plane waves can be injected from both sides in order to construct the scattering state. The dashed gray line shows that the height of the barrier was slightly extended (and contracted) in order to calculate Q_n .

matrix, which is already given in Eqs. (3.2) and (3.3) and is repeated below for the sake of clarity:

$$S_{11} = S_{22} = -\frac{e^{-2ikL}(-1 + e^{4ikLn})(n^2 - 1)}{e^{4ikLn}(n-1)^2 - (n+1)^2}, \quad (3.39)$$

$$S_{12} = S_{21} = -\frac{4e^{2ikL(n-1)}n}{e^{4ikLn}(n-1)^2 - (n+1)^2}. \quad (3.40)$$

The components of Q_n are then

$$Q_{n,11} = Q_{n,22} = \frac{-8kL(n^3 + n) - 2(n^2 - 1)\sin(4kLn)}{-(n^2 + 6)n^2 + (n^2 - 1)^2 \cos(4kLn) - 1}, \quad (3.41)$$

$$Q_{n,12} = Q_{n,21} = \frac{-8kLn(n^2 - 1)\cos(2kLn) - 4(n^2 + 1)\sin(2kLn)}{-(n^2 + 6)n^2 + (n^2 - 1)^2 \cos(4kLn) - 1}. \quad (3.42)$$

The solution of the eigenproblem associated to Q_n is

$$\theta_n^1 = \frac{-4kLn - 2\sin(2kLn)}{(n^2 - 1)\cos(2kLn) - n^2 - 1}, \quad \mathbf{u}_n^1 = \frac{1}{\sqrt{2}} \begin{pmatrix} 1 \\ 1 \end{pmatrix}, \quad (3.43)$$

$$\theta_n^2 = \frac{4kLn - 2\sin(2kLn)}{(n^2 - 1)\cos(2kLn) + n^2 + 1}, \quad \mathbf{u}_n^2 = \frac{1}{\sqrt{2}} \begin{pmatrix} -1 \\ 1 \end{pmatrix}. \quad (3.44)$$

The intensities integrated over length of the potential barriers are

$$I_1 \equiv \int_{-L}^L |\psi(\mathbf{u}_n^1)|^2 dx = \frac{-4kLn - 2\sin(2kLn)}{kn[(n^2 - 1)\cos(2kLn) - n^2 - 1]},$$

$$I_2 \equiv \int_{-L}^L |\psi(\mathbf{u}_n^2)|^2 dx = \frac{4kLn - 2\sin(2kLn)}{kn[(n^2 - 1)\cos(2kLn) + n^2 + 1]}, \quad (3.45)$$

where the argument in the parentheses indicates which eigenvector of Q_n is injected into the system. From these expressions it is easy to see that there is a strict linear relation between I_i and θ_n^i :

$$\frac{I_1}{\theta_n^1} = \frac{I_2}{\theta_n^2} = \frac{1}{kn}. \quad (3.46)$$

This concludes the proof and fixes the proportionality constant of the direct linear relation to $1/(kn)$.

In two dimensions the analytical expression of Q_n cannot be given, however, we are able to show that the intensity integrated over the area A of the target,

$$I(\mathbf{u}_n^i) \equiv \int |\psi(\mathbf{u}_n^i)|^2 dA, \quad (3.47)$$

is in a strict linear relation with the eigenvalues of Q_n , i.e.,

$$I(\mathbf{u}_n^i) = \frac{\theta_n^i}{nk^2}, \quad (3.48)$$

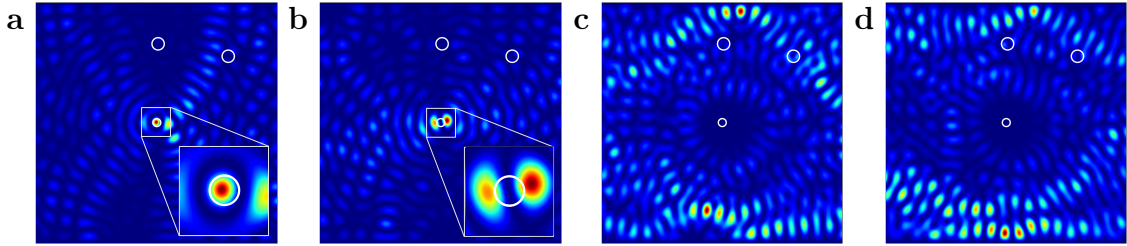


Fig. 3.12. Numerical simulation in the waveguide setup with a Teflon target (radius $R = 0.0165W$, refractive index $n = 1.44$). The number of propagating modes used is $N = 20$ and the wavelength is $\lambda = 0.1W$. **a, b**, Spatial intensity distribution of the two Q_n -eigenstates with the largest eigenvalues θ_n . A strong focus onto the inside of the target scatterer can be clearly observed. **c, d**, Spatial intensity distribution of the two Q_n -eigenstates with the smallest eigenvalues θ_n , showing a strong avoidance of the target scatterer.

where we fix the proportionality constant by dimensional analysis. We empirically verify this result in Fig. 3.6a. In Fig. 3.12 we show the spatial intensity distribution of scattering states corresponding to the largest and smallest eigenvalues of Q_n . One can clearly observe the strong focus achieved by the scattering states associated to large eigenvalues and the avoidance of the target by the scattering states associated to small eigenvalues. This allows us to smoothly tune the degree of focusing over several orders of magnitude by choosing superpositions of eigenstates with large or small eigenvalues – ranging from perfect focus to complete avoidance. To support our claim of optimal focus we compare our approach to an established method for optimal focus [73] in section 4.1 and show that our technique indeed also gives the optimal focus onto a point. Our method, however, surpasses the method given in Ref. [73] when we consider focusing into an extended area.

Chapter 4.

Discussion

In this chapter we discuss the results achieved so far. We start by showing that we indeed achieve an optimal focus by comparing our approach to an already existing technique that was developed specifically for that purpose. Moreover, we demonstrate that the different realizations of the GWS-operator can be used as building blocks for more complex applications, like transferring linear momentum in an arbitrary direction, constructing two different methods for an optical trap or for applying torque to a target while maintaining its position. We will also discuss the situation where we do not consider the ideal case with a Hermitian operator Q_α but a non-ideal one taking into account experimental restrictions to show that our ideas also work in envisioned experimental realizations.

4.1. Comparing the GWS-Focus to the Field Matrix Method

In Ref. [73] the authors use the field matrix $e(x)$ to achieve optimal focus onto a point inside a scattering medium. This matrix with components $e_{ba}(x)$ relates the field inside the medium at depth x and transverse position b , $E_b(x)$, to the field in the leads at the transverse position a , E_a , i.e., $E_b(x) = \sum_a e_{ba}(x)E_a$. In order to focus in an optimal way onto a target point β , one needs to construct a scattering state at the input as

$$E_a^{\text{opt}} = e_{\beta a}^* I_\beta^{-1/2}(x), \quad (4.1)$$

where $I_\beta(x) = \sum_a |e_{\beta a}(x)|^2$ normalizes the input vector and $*$ denotes complex conjugation. This claim was proven in Ref. [74] for the case of a focus behind a scattering medium utilizing the transmission matrix t . For the sake of completeness, we give this proof in the following. The field inside the scattering medium at the transverse position β is given by

$$E_\beta(x) = \sum_{a=1}^N e_{\beta a}(x)E_a, \quad (4.2)$$

where E_a is the field in the leads and N is the number of incident channels. Maximizing the field's intensity at β is equivalent to maximizing $|E_\beta(x)|$. This quantity has an upper bound given by the Cauchy-Schwarz inequality, i.e.,

$$|E_\beta(x)| \leq \sum_{a=1}^N |e_{\beta a}(x)| |E_a|. \quad (4.3)$$

This upper bound is reached if and only if $E_a = C e_{\beta a}^*$, where C is an arbitrary complex constant. Thus, the input field for maximizing the intensity at β is given by

$$E_a^{\text{opt}} = C e_{\beta a}^*. \quad (4.4)$$

C is fixed by the condition that the incident intensity is normalized to one, i.e.,

$$\sum_a^N |E_a^{\text{opt}}|^2 = \sum_a^N |C e_{\beta a}^*|^2 = 1. \quad (4.5)$$

Resolving for C gives

$$C = \left(\sum_a^N |e_{\beta a}|^2 \right)^{-1/2} \equiv I_\beta^{-1/2}. \quad (4.6)$$

In Fig. 4.1a we compare the field matrix method, which maximizes the intensity at a certain point with the highest Q_n -eigenstate, which maximizes the intensity in the target area where the refractive index n is varied. The waveguide geometry in which we contrast the two methods is the same as in section 3.4. The target has a diameter of $D = 0.033W$, with W being the width of the waveguide, and is thus slightly smaller than half the wavelength $\lambda_s \equiv \lambda/n \approx 0.07W$ inside the scatterer. As long as this condition is fulfilled, we observe that the state calculated with the field matrix method and the highest Q_n -eigenstate are in excellent agreement with each other, featuring a single peak inside the target area (see Fig. 4.1b). For a diameter larger than this limit, i.e., $D \geq 0.5\lambda_s$, the highest Q_n -eigenstate forms two peaks inside the target area in order to maximize the stored intensity (see Fig. 4.1c), while the field matrix method still only gives a single peak at the target's center. This single peak has the consequence that the integrated intensity inside the target is approximately 0.4 times lower than that of the highest Q_n -eigenstate. In principle, maximizing the intensity in such an extended area would also be possible with the field matrix method, but one would have to find the required multiple focus spots via an iterative optimization procedure.

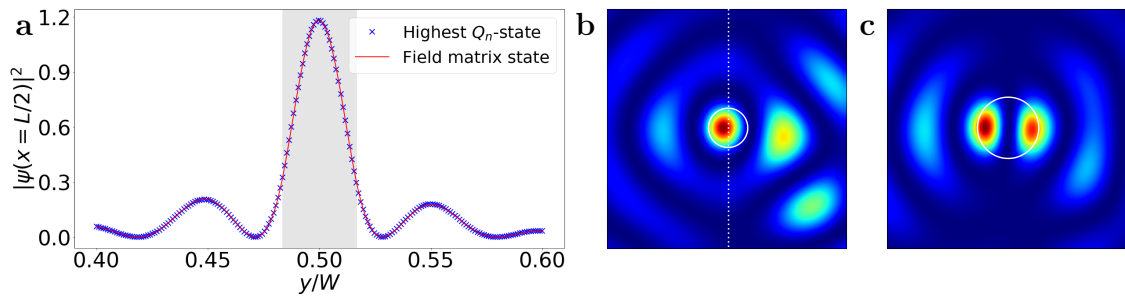


Fig. 4.1. **a**, Intensity distribution at $x = L/2$ along the transverse coordinate y for the field matrix state and the highest Q_n -eigenstate, which are identical due to the small size of the target's diameter $D = 0.33W = 0.48\lambda_s = 0.48\lambda/n$. In case of the field matrix state, we calculated the field matrix $e_{\beta,a}$ at $x = L/2$ and set $\beta = W/2$. The gray shaded region marks the target scatterer. **b**, Spatial intensity distribution of the highest Q_n -eigenstate in an area around the target scatterer, which is identical to intensity distribution of the field matrix state. The dashed line indicates at which position the cut in **a** was made. **c**, Spatial intensity distribution of the highest Q_n -eigenstate for a target with diameter $D = 0.75\lambda_s$. In order to maximize the stored intensity, the state features two peaks inside the target. This allows the highest Q_n -eigenstate to have an integrated intensity inside the target that is 2.5 times higher than the integrated intensity of the field matrix-state for this configuration, which is calculated to still focus onto the target's center.

4.2. Pushing a Target in an Arbitrary Direction

One application, that shows the strength of the GWS-concept is the ability to push a target in an arbitrary direction in a disordered medium. As a model system we once again use the waveguide geometry depicted in Fig. 3.1, where the target is in this case a metallic circle of radius $R = 0.0825W$.

In Ref. [60] it was shown that an eigenstate of the GWS-operator Q_x , i.e., the GWS-operator for a shift of a target in the longitudinal direction, has a well defined momentum transfer onto that target in the direction of the shift, x . It does not, however, carry information about the momentum transfer in the orthogonal direction to x , i.e., y , which can be even larger than the momentum transfer in longitudinal direction. In the following we will show how to construct a superposition of Q_x -eigenstates that have a drastically reduced momentum transfer in the y -direction, which enables us to push a target into a certain direction without a push in an unwanted direction.

This is achieved by taking two Q_x -eigenstates, \mathbf{u}_x^1 and \mathbf{u}_x^2 (depicted in Fig. 4.2), with a large parallel momentum transfer in the longitudinal direction. To reduce the momentum transfer in the orthogonal direction, we have further chosen eigenstates which also feature a transversal momentum transfer of opposite signs, which

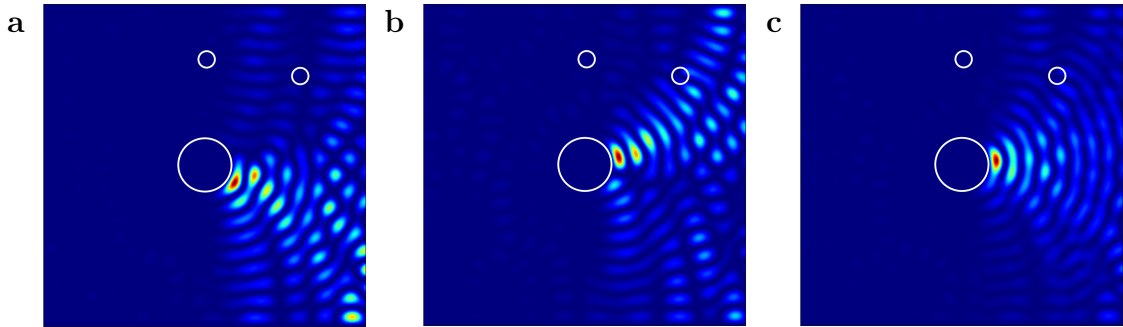


Fig. 4.2. Numerical simulation in the waveguide setup depicted in Fig. 3.1 with a metallic target (radius $R = 0.0825W$), a wavelength of $\lambda \approx 0.1W$ and $N = 20$ open modes. **a, b**, Spatial intensity distribution of two Q_x -eigenstates, \mathbf{u}_x^1 and \mathbf{u}_x^2 , whose superposition, is used to create a scattering state that transfers momentum only in the x -direction with no momentum transfer into the orthogonal y -direction. Both states push the target to the left, while the one in the left (middle) plot pushes the central scatterer also upwards (downwards). **c**, Spatial intensity distribution of the scattering state $\mathbf{s} = c\mathbf{u}_x^1 + \mathbf{u}_x^2$, where $c \in \mathbb{R}$ is calculated using a root finding algorithm solving $\mathbf{s}^\dagger Q_y \mathbf{s} = 0$, i.e., the transversal momentum transfer onto the target is minimized. In this scattering geometry, the transversal momentum transfer is damped by a factor of 10^4 .

is calculated via the expectation value of the corresponding GWS-operator Q_y , i.e., $(\mathbf{u}_x^{1,2})^\dagger Q_y \mathbf{u}_x^{1,2}$. We then construct a superposition $\mathbf{s} = c\mathbf{u}_x^1 + \mathbf{u}_x^2$, with $c \in \mathbb{R}$, where c is calculated by solving $\mathbf{s}^\dagger Q_y \mathbf{s} = 0$ using a root finding algorithm. This gives us a state that transfers momentum in a certain direction with minimal unwanted orthogonal contributions. The spatial intensity distribution for such a state \mathbf{s} is depicted in Fig. 4.2c. It is clear from a quick glance that the incident angle is exactly in the longitudinal direction.

Momentum transfer into an arbitrary direction can easily be achieved by shifting the target scatterer in any direction [60]. There is, however, a second method for constructing a GWS-operator that allows to control the momentum transfer in an arbitrary direction. It is given by the linear combination of two GWS-operators that were calculated by considering shifts in orthogonal directions, like Q_x and Q_y , i.e.,

$$Q_{a,b} = \frac{1}{\sqrt{a^2 + b^2}} (aQ_x + bQ_y), \quad (4.7)$$

where the vector $(a, b)^T$ tells us the direction into which the eigenstates of $Q_{a,b}$ transfer momentum. This claim is verified by numerical simulations shown in Fig. 4.3a. Next we show in Fig. 4.3b that the eigenvalues of $Q_{a,b}$ are exactly the same as the eigenvalues of the GWS-operator we get by shifting the target in the direction of $(a, b)^T$. In Fig. 4.3c we show the spatial intensity distribution of the largest $Q_{3,1}$ -

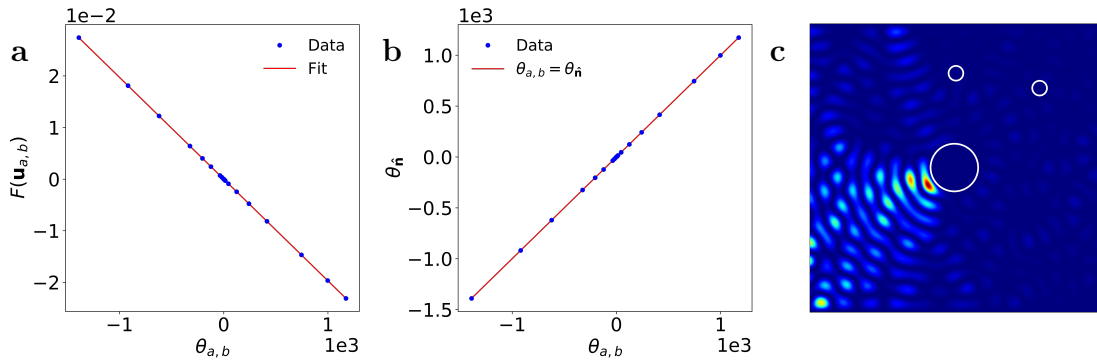


Fig. 4.3. Numerical evidence that a momentum transfer into an arbitrary direction $(a, b)^T$ can be achieved by superimposing two orthogonal shift GWS-operators, e.g. $Q_{a,b} \propto aQ_x + bQ_y$. **a**, Linear relation between between the eigenvalues $\theta_{a,b}$ of $Q_{a,b}$ and the applied force in direction of $(a, b)^T = (3, 1)^T$. The deviation from perfect correlation is 10^{-7} . **b**, Linear relation between the eigenvalues $\theta_{a,b}$ and the eigenvalues of $Q_{\hat{n}}$, i.e., the GWS-operator we get when shifting the target in direction of $\hat{n} = (3, 1)^T / \sqrt{10}$. These eigenvalues are the same up to a mean squared error of the order of 10^{-10} . **c**, Spatial intensity distribution of the $Q_{a,b}$ -eigenstate that corresponds to the eigenvalue with the largest magnitude, i.e., $|\theta_{a,b}|$. One can see that the incident angle is approximately 18° with the waveguide's walls, which is the angle we want when choosing $(a, b) = (3, 1)$.

eigenstate with $(a, b)^T = (3, 1)^T$. One can see that the incidence angle is about 18° with the waveguide's walls, which is the same angle as that of $(a, b)^T = (3, 1)^T$ with the waveguide's walls. This empirically confirms that $Q_{a,b}$ is a suitable choice when one wants to shift a target in an arbitrary direction.

4.3. Optical Trapping

In this section we show two realizations of an optical trap that can be realized with GWS-operators and also compare them with each other. The concepts are once again demonstrated in the waveguide geometry depicted in Fig. 3.1.

Both concepts rely on minimization of the following quantity,

$$[(\mathbf{s}^\dagger Q_x \mathbf{s})^2 + (\mathbf{s}^\dagger Q_y \mathbf{s})^2]^{1/2} \rightarrow \min, \quad (4.8)$$

which measures the magnitude of the total momentum transferred onto the target of a linear superposition \mathbf{s} of GWS-eigenstates.

The first idea uses the eigenstates of Q_x as introduced in section 3.1. In the first step we select the four eigenstates of Q_x that contain all four possible sign combinations for longitudinal and transversal momentum transfer and whose momentum

transfer's magnitude is as large as possible. In the second step we construct a superposition out of those four states, i.e., $\mathbf{s} = \sum_{i=1}^4 c_i \mathbf{u}_x^i$, with $c_i \in \mathbb{R}$. The c_i are calculated using an optimization algorithm minimizing Eq. (4.8), i.e., the total momentum transfer onto the target. The spatial intensity distribution of the resulting state \mathbf{s} is shown in Fig. 4.4b. One can see the wave intensity building up on almost the whole boundary of the target, resulting in a tight trapping.

The second idea utilizes a superposition, $\mathbf{t} = \sum_{i=1}^4 d_i \mathbf{u}_R^i$, of eigenstates of Q_R . The eigenstates are selected using similar criteria as in the preceding paragraph, i.e., they need to have opposite momentum transfer in the longitudinal and transversal direction (calculated using expectation values of Q_x and Q_y), while their eigenvalues θ_R should be as large as possible. The d_i are calculated using an optimization algorithm minimizing Eq. (4.8) when replacing \mathbf{s} by \mathbf{t} , i.e., the total momentum transfer onto the target. The spatial intensity distribution of the resulting state \mathbf{t} is depicted in Fig. 4.4c, depicting an intensity build-up on four points along the boundary of the target, resulting in a tight trapping.

In order to compare these two ideas, we displace the target longitudinally and transversally while injecting the same scattering state \mathbf{s} and \mathbf{t} , respectively, and

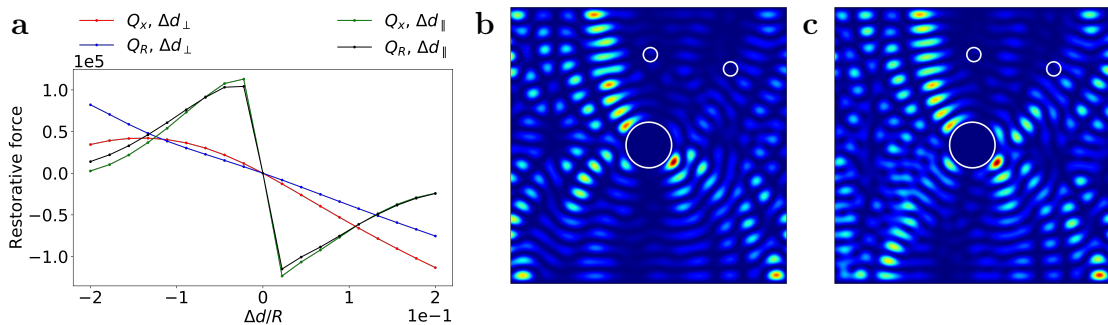


Fig. 4.4. Two different realizations for the use of the GWS-concept as an optical trap. **a**, Restorative force experienced by the target, pushing it back in direction of the displacement plotted over the displacement normalized to the target's radius R . Δd_{\perp} (Δd_{\parallel}) denotes that the displacement happened in transversal (longitudinal) direction. The optical trap is stiffer (measured by the greater slope at $\Delta d = 0$) when the displacement happens in longitudinal direction, because the waveguide's walls make it harder for the wave to provide a restorative force from below or above. **b**, Spatial intensity distribution of the state $\mathbf{s} = \sum_{i=1}^4 c_i \mathbf{u}_x^i$, where the $c_i \in \mathbb{R}$ are calculated using an optimization algorithm minimizing $[(\mathbf{s}^{\dagger} Q_x \mathbf{s})^2 + (\mathbf{s}^{\dagger} Q_y \mathbf{s})^2]^{1/2}$ and the \mathbf{u}_x^i are eigenstates of Q_x . This state has a ratio $t_s = 3.5 \times 10^{-5}$. **c**, Spatial intensity distribution of the state $\mathbf{t} = \sum_{i=1}^4 d_i \mathbf{u}_R^i$, where the $d_i \in \mathbb{R}$ are calculated using an optimization algorithm minimizing $[(\mathbf{t}^{\dagger} Q_x \mathbf{t})^2 + (\mathbf{t}^{\dagger} Q_y \mathbf{t})^2]^{1/2}$ and the \mathbf{u}_R^i are eigenstates of Q_R . This state has a ratio $t_s = 5.6 \times 10^{-5}$.

calculate the restorative force using Eq. (3.18) in dependence of the displacement Δd . The result for this consideration is depicted in Fig. 4.4a, showing that these two ideas are of comparable capability. To classify their initial trapping strength we compute the ratio $t_s \equiv |F|/P$, which is the total momentum transfer's magnitude divided by the pressure.

4.4. Applying Torque without Linear Momentum Transfer

In section 3.3.1 we show how to transfer torque onto a metallic target using Q_φ , whose eigenvalues θ_φ quantify the amount of torque transferred. These eigenvalues, however, carry no information about the linear momentum transfer that inevitably accompanies such an exertion of torque. As is evident from Figs. 4.5a and 4.5b the eigenstates \mathbf{u}_φ of Q_φ also transfer a considerable amount of momentum onto the target and thus push it in a certain direction, because the intensity build-up is mainly on one side. In this section we develop a protocol that allows us to apply torque onto a target, ideally near the theoretical maximum, while simultaneously holding it in place, like in an optical trap. We investigate this protocol in the waveguide geometry that is shown in Fig. 3.1.

All we need for this protocol are the GWS-operators Q_x and Q_y , as introduced in section 4.2 and Q_φ as introduced in section 3.3.1. We select two eigenstates of Q_φ that apply as much torque as possible onto the target and have a longitudinal and transversal momentum transfer of opposite signs, which are measured via the expectation values of Q_x and Q_y . Out of those two states we construct a superposition

$$\mathbf{s} = c_1 \mathbf{u}_\varphi^1 + c_2 \mathbf{u}_\varphi^2, \quad (4.9)$$

where the coefficients $c_i \in \mathbb{C}$ are calculated using an optimization algorithm minimizing Eq. (4.8), i.e., the magnitude of the total momentum transferred onto the target. The spatial intensity distributions of the resulting state \mathbf{s} and its constituents \mathbf{u}_φ^1 and \mathbf{u}_φ^2 are shown in Fig. 4.5. One can see that the state \mathbf{s} focuses onto opposite sides of the square such that a sizeable torque but only minimal linear momentum is transferred. Note that this procedure can be generalized to more general superpositions of Q_φ -eigenstates.

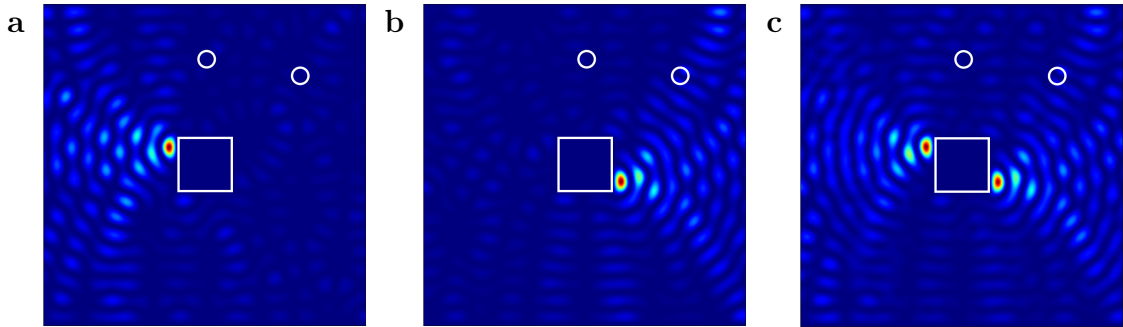


Fig. 4.5. **a, b**, Spatial intensity distribution of two Q_φ -eigenstates, \mathbf{u}_1 and \mathbf{u}_2 . It is evident from a quick glance that in the left (middle) picture clockwise torque is applied onto the target while also pushing it to the left (right). **c**, Spatial intensity distribution of the state defined in Eq. (4.9), constructed out of the Q_φ -eigenstates shown in **a** and **b**. The coefficients $c_i \in \mathbb{C}$ are calculated minimizing $[(\mathbf{s}^\dagger Q_x \mathbf{s})^2 + (\mathbf{s}^\dagger Q_y \mathbf{s})^2]^{1/2}$, i.e., the linear momentum transfer's magnitude that inevitably accompanies a Q_φ -eigenstate, using an optimization algorithm. In this setup, these unwanted contributions could be reduced by a factor of 10^2 . By combining different Q_φ -eigenstates it is therefore possible to apply torque onto a target while transferring a minimized amount of linear momentum.

4.5. Non-Ideal Conditions

So far we have only demonstrated the capabilities of the GWS-operator in a setting where we have full access to the unitary scattering matrix S , resulting in a Hermitian operator Q_α featuring real eigenvalues. If we want to show that our concept also works in the experiment we have to study our ideas also in the subunitary regime, where we only have access to a subpart of the scattering matrix S . In order to give one example that the GWS-concept also works in the subunitary regime, we consider the same waveguide as depicted in Fig. 3.1, but now fill it with 300 randomly distributed Teflon scatterers and one square metallic target scatterer. We change the set-up compared to previous chapters to increase the total reflectivity of the system. The necessity of this step will be made clear below. In order to get into the subunitary regime we consider only the reflection matrix r , which is accessible in many experiments. Furthermore, to simulate a low numerical aperture, we cut the M highest modes out of r such that we are left with a $(N - M) \times (N - M)$ -dimensional matrix \tilde{r} , where N is the number of modes in the waveguide. The subunitary regime of the GWS-operator was already studied in [60], where it is shown in the supplementary material that the eigenvalues of the GWS-operator built from only a subpart of the scattering matrix, $q_\varphi = -ir^{-1}dr/d\varphi$ are

$$\theta_\varphi^i \propto M_z(\mathbf{u}_\varphi^i) - i\mathbf{u}_\varphi^{i,\dagger} t^\dagger \frac{dt}{d\varphi} \mathbf{u}_\varphi^i \quad (4.10)$$

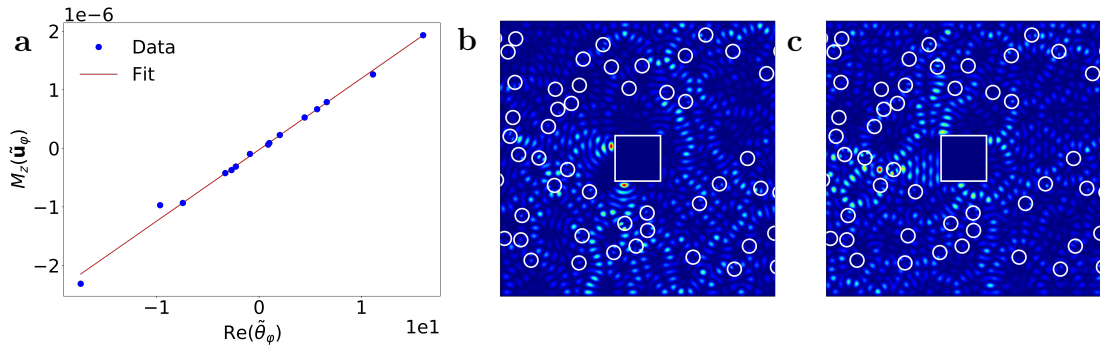


Fig. 4.6. Numerical simulation of the waveguide setup filled with 300 randomly distributed Teflon scatterer (radius $R = 0.025W$, refractive index $n = 1.44$) and a metallic square target (side length $0.165W$) at x -position $L/6$. The number of propagating modes used is $N = 40$, we discard the $M = 10$ highest modes in order to simulate a low numerical aperture and the wavelength is $\lambda \approx 0.05W$. In the SVD-procedure we project on the 15 highest reflecting states in order to select states with low transmission. **a**, Linear relation between the real part of \tilde{q}_φ 's eigenvalues and the total torque transferred onto the target scatterer. The correlation coefficient is $r = 0.997$ which shows that this concept still works in non-ideal conditions. **b**, **c**, Spatial intensity distribution of two \tilde{q}_φ -eigenstates with the largest absolute value of $\text{Re}(\tilde{\theta}_\varphi)$. A strong focusing on the corners of the target scatterer, evidently transferring torque, can be clearly observed.

with t being the transmission matrix. Note that in [60] the analogous case of a GWS-operator built out of the transmission matrix t was considered. The loss of information due to the venture into the subunitary regime manifests itself in complex eigenvalues due to the second term, which is not available in our approach. In order to minimize the second term and to still maintain a relation between the eigenvalues θ_φ and the total torque M_z we use a projection of \tilde{r} onto highly reflecting channels by means of a singular value decomposition (SVD) of the reflection matrix $\tilde{r} = U\Sigma V^\dagger$. The unitary matrices U and V contain column-wise the left and right singular vectors and the matrix $\Sigma = \text{diag}(\{\sigma_n\})$ contains the singular values on its diagonal. In order to project onto the highly reflecting states we select a subset of large singular values $\tilde{\Sigma} = \text{diag}(\{\tilde{\sigma}_n\})$ with corresponding left and right singular vectors stored in \tilde{U} and \tilde{V} . Equipped with these tools we can construct an effective inverse $\tilde{r}^{-1} = \tilde{V}(\tilde{U}^\dagger \tilde{r} \tilde{V})^{-1} \tilde{U}^\dagger = \tilde{V} \tilde{\Sigma}^{-1} \tilde{U}^\dagger$. We also need to project the derivative of \tilde{r} onto this subspace with the proper projection operators $P_{\tilde{U}} = \tilde{U} \tilde{U}^\dagger$ and $P_{\tilde{V}} = \tilde{V} \tilde{V}^\dagger$. We then arrive at the following expression for the GWS-operator

$$\tilde{q}_\varphi = -i \tilde{V} (\tilde{U}^\dagger \tilde{r} \tilde{V})^{-1} \tilde{U}^\dagger \tilde{U} \tilde{U}^\dagger \frac{d\tilde{r}}{d\varphi} \tilde{V} \tilde{V}^\dagger. \quad (4.11)$$

In Fig. 4.6 we show the spatial intensity distribution of the two \tilde{q}_φ -eigenstates that transfer the largest torque onto the target. It is clearly observable that there is an intensity build-up at the corners of the target, such that torque is transferred onto it. In Fig. 4.6a we show the relation (3.35) which is still almost perfectly fulfilled. This result strongly suggests that we can use all GWS-operators in the subunitary regime.

Chapter 5.

Summary

In this thesis we present a whole class of operators that allows us to manipulate a target inside a disordered system in many different ways. These GWS-operators Q_α , are based on the Wigner-Smith time-delay operator. Depending on the choice of the parameter α we can perform different tasks. The first choice for the parameter α is the position of the target, which we want to manipulate, allowing us to control the force applied to it. We also study the GWS-operator we get by considering the radius of the target as the parameter α , enabling us to apply a well-defined pressure onto it. Moreover, we can control the torque exerted onto the target by considering the orientation angle of a non-circular target as the parameter. Last but not least, we use the refractive index of the target as the parameter α to control the total intensity, i.e., the degree of focusing, inside the target [75]. Our technique allows us to smoothly tune the respective quantity transferred to the target over several orders of magnitude. We want to emphasize here that the presented techniques are applicable to dielectric as well as to metallic targets and for almost any shapes and sizes.

We also show that we are able to achieve the theoretical maximum of transferred force, pressure or torque onto the target as well as the optimal focus in the target. Especially finding the best focus onto a certain spot is a task that has challenged researchers over the last decades. We compare our approach to an already existing technique and confirm that we are indeed able to achieve this optimal focus.

The key feature of our concept is that the four different GWS-operators we have studied can be used as a toolbox of building blocks for more sophisticated applications. We show how push a target into an arbitrary direction and discuss two different realizations of an optical trap. Finally we present a method for transferring torque onto it without any linear momentum transfer, i.e., we can rotate a target without pushing it into one direction.

In order to show that an envisioned experimental realization in the optical or microwave regime is a worthwhile endeavor, we numerically confirm that our technique is still applicable when considering experimental imperfections such as low numerical aperture and limited access to the scattering matrix.

All of the above mentioned investigations have been carried out in a two di-

mensional waveguide model in which the propagation of electromagnetic waves is described by the Helmholtz equation. Due to its structural similarity to the Schrödinger equation, we conclude that all these approaches are also valid in the context of quantum mechanics. Since the GWS-operator involves only the system's scattering matrix S and its derivative with respect to the parameter α , we believe that our approach for micromanipulation is universally applicable to linear systems that can be characterized by a scattering matrix S .

We conclude this thesis with an outlook on further research. The Wigner-Smith time-delay operator shares a deep connection with the density of states of an open scattering system [76, 77]. We want to investigate this connection also for the GWS-operator and we expect to gain new physical insight such as certain invariance properties of a scattering systems. Although we have shown that our GWS-concept can be applied under experimental limitations, there are still some other factors, such as absorption, that have to be considered. Furthermore, we plan to investigate in which way GWS-eigenstates that focus onto an object in a disordered medium can be used to reconstruct an image of this object.

The promising numerical results in this thesis pave the way for new methods of micromanipulation of an embedded object as well as for focusing onto a target. In the long run could this lead to exciting applications, especially in biomedical imaging. The technique for optimal focus presented in this thesis is particularly elegant. Our method also gives the theoretical maximum for applied force, pressure and torque onto a target, which is – at least to the best of our knowledge – the first time this has been achieved.

Appendix A.

Statistical Tools

A.1. Correlation Coefficient

Given two variables X and Y , we can find the degree of linear correlation between them by calculating Pearson's correlation coefficient $r \in [-1, 1]$. $r = 1$ and $r = -1$ refer to total positive or negative correlation respectively, while $r = 0$ means no correlation at all. For a sample of size n , r is calculated by

$$r = \frac{\sum_{i=1}^n (x_i - \bar{x})(y_i - \bar{y})}{\sqrt{\sum_{i=1}^n (x_i - \bar{x})^2} \sqrt{\sum_{i=1}^n (y_i - \bar{y})^2}}, \quad (\text{A.1})$$

where x_i and y_i are the individual sample points and \bar{x} and \bar{y} are the corresponding mean values. We measure deviation from perfect positive or negative correlation by computing,

$$\Delta r \equiv \pm 1 - r. \quad (\text{A.2})$$

A.2. Mean Squared Error

Given two vectors \tilde{Y} and Y , where \tilde{Y} contains the predictions and Y the observed values then the mean-squared error (MSE) of the predictor is computed as

$$\text{MSE} = \frac{1}{n} \sum_{i=1}^n (\tilde{y}_i - y_i)^2, \quad (\text{A.3})$$

where n is the number of data points and \tilde{y}_i and y_i are the individual sample points.

Acknowledgments

I want to conclude this thesis by acknowledging and expressing my deep gratitude to a few people that made it possible to carry out this work.

- My thesis advisor Prof. Dr. Stefan Rotter, who provided me a very fruitful topic for my master's thesis and who was always open for questions and discussions, deepening my physical understanding.
- My thesis co-advisor Dipl.-Ing. Matthias Kühmayer, who always had an open ear for my questions, helping me out a lot and shared and explained his computer code to me.
- My thesis co-advisor Dipl.-Ing. Andre Brandstötter, whom I also could ask anything anytime, which was invaluable for my progress. I am also grateful that he dedicated a lot of time to proof-reading and improving my writing.
- Prof. Dr. Florian Libisch for providing and helping me with his computer code, which was a valuable asset for conducting this research.
- My parents Sonja and Andreas Horodynski and my godparents Elisabeth and Waldemar Mooslechner for their unconditional financial and moral support, allowing me to freely pursue my studies.

Bibliography

- [1] A. Ashkin, J. M. Dziedzic, J. E. Bjorkholm, and S. Chu, “Observation of a single-beam gradient force optical trap for dielectric particles,” *Optics Letters*, vol. 11, p. 288, May 1986.
- [2] A. Ashkin, J. M. Dziedzic, and T. Yamane, “Optical trapping and manipulation of single cells using infrared laser beams,” *Nature*, vol. 330, pp. 769–771, Dec. 1987.
- [3] K. Dholakia and P. Reece, “Optical micromanipulation takes hold,” *Nano Today*, vol. 1, pp. 18–27, Feb. 2006.
- [4] K. C. Neuman and S. M. Block, “Optical trapping,” *Review of Scientific Instruments*, vol. 75, pp. 2787–2809, Sept. 2004.
- [5] G. Thalhammer, R. Steiger, S. Bernet, and M. Ritsch-Marte, “Optical macro-tweezers: trapping of highly motile micro-organisms,” *Journal of Optics*, vol. 13, p. 044024, Apr. 2011.
- [6] R. Bowman, A. Jesacher, G. Thalhammer, G. Gibson, M. Ritsch-Marte, and M. Padgett, “Position clamping in a holographic counterpropagating optical trap,” *Optics Express*, vol. 19, p. 9908, May 2011.
- [7] T. Franosch, M. Grimm, M. Belushkin, F. M. Mor, G. Foffi, L. Forró, and S. Jeney, “Resonances arising from hydrodynamic memory in Brownian motion,” *Nature*, vol. 478, pp. 85–88, Oct. 2011.
- [8] A. Jannasch, M. Mahamdeh, and E. Schäffer, “Inertial Effects of a Small Brownian Particle Cause a Colored Power Spectral Density of Thermal Noise,” *Physical Review Letters*, vol. 107, Nov. 2011.
- [9] D. Palima and J. Glückstad, “Gearing up for optical microrobotics: micromanipulation and actuation of synthetic microstructures by optical forces: Gearing up for optical microrobotics,” *Laser & Photonics Reviews*, vol. 7, pp. 478–494, July 2013.
- [10] S. Kheifets, A. Simha, K. Melin, T. Li, and M. G. Raizen, “Observation of Brownian Motion in Liquids at Short Times: Instantaneous Velocity and Memory Loss,” *Science*, vol. 343, pp. 1493–1496, Mar. 2014.

-
- [11] T. Li, “Millikelvin Cooling of an Optically Trapped Microsphere in Vacuum,” in *Fundamental Tests of Physics with Optically Trapped Microspheres*, pp. 81–110, New York, NY: Springer New York, 2013.
- [12] H. He, M. E. J. Friese, N. R. Heckenberg, and H. Rubinsztein-Dunlop, “Direct Observation of Transfer of Angular Momentum to Absorptive Particles from a Laser Beam with a Phase Singularity,” *Physical Review Letters*, vol. 75, pp. 826–829, July 1995.
- [13] M. E. J. Friese, J. Enger, H. Rubinsztein-Dunlop, and N. R. Heckenberg, “Optical angular-momentum transfer to trapped absorbing particles,” *Physical Review A*, vol. 54, pp. 1593–1596, Aug. 1996.
- [14] M. E. J. Friese, T. A. Nieminen, N. R. Heckenberg, and H. Rubinsztein-Dunlop, “Optical alignment and spinning of laser-trapped microscopic particles,” *Nature*, vol. 394, pp. 348–350, July 1998.
- [15] A. I. Bishop, T. A. Nieminen, N. R. Heckenberg, and H. Rubinsztein-Dunlop, “Optical application and measurement of torque on microparticles of isotropic nonabsorbing material,” *Physical Review A*, vol. 68, Sept. 2003.
- [16] E. Higurashi, H. Ukita, H. Tanaka, and O. Ohguchi, “Optically induced rotation of anisotropic micro-objects fabricated by surface micromachining,” *Applied Physics Letters*, vol. 64, pp. 2209–2210, Apr. 1994.
- [17] N. B. Simpson, K. Dholakia, L. Allen, and M. J. Padgett, “Mechanical equivalence of spin and orbital angular momentum of light: an optical spanner,” *Optics Letters*, vol. 22, p. 52, Jan. 1997.
- [18] T. Asavei, V. L. Y. Loke, M. Barbieri, T. A. Nieminen, N. R. Heckenberg, and H. Rubinsztein-Dunlop, “Optical angular momentum transfer to microrotors fabricated by two-photon photopolymerization,” *New Journal of Physics*, vol. 11, p. 093021, Sept. 2009.
- [19] T. Čižmár, M. Mazilu, and K. Dholakia, “In situ wavefront correction and its application to micromanipulation,” *Nature Photonics*, vol. 4, pp. 388–394, June 2010.
- [20] K. Dholakia and T. Čižmár, “Shaping the future of manipulation,” *Nature Photonics*, vol. 5, pp. 335–342, June 2011.
- [21] N. Savage, “Digital spatial light modulators,” *Nature Photonics*, vol. 3, no. 3, p. 170, 2009.
- [22] S. Rotter and S. Gigan, “Light fields in complex media: Mesoscopic scattering meets wave control,” *Reviews of Modern Physics*, vol. 89, Mar. 2017.

-
- [23] I. M. Vellekoop and A. P. Mosk, "Focusing coherent light through opaque strongly scattering media," *Optics Letters*, vol. 32, p. 2309, Aug. 2007.
- [24] E. G. van Putten, D. Akbulut, J. Bertolotti, W. L. Vos, A. Lagendijk, and A. P. Mosk, "Scattering Lens Resolves Sub-100 nm Structures with Visible Light," *Physical Review Letters*, vol. 106, May 2011.
- [25] S. Popoff, G. Lerosey, M. Fink, A. C. Boccara, and S. Gigan, "Image transmission through an opaque material," *Nature Communications*, vol. 1, pp. 1–5, Sept. 2010.
- [26] R. Horstmeyer, H. Ruan, and C. Yang, "Guidestar-assisted wavefront-shaping methods for focusing light into biological tissue," *Nature Photonics*, vol. 9, pp. 563–571, Sept. 2015.
- [27] I. M. Vellekoop, E. G. van Putten, A. Lagendijk, and A. P. Mosk, "Demixing light paths inside disordered metamaterials," *Optics Express*, vol. 16, no. 1, p. 67, 2008.
- [28] I. M. Vellekoop and C. M. Aegerter, "Scattered light fluorescence microscopy: imaging through turbid layers," *Optics Letters*, vol. 35, p. 1245, Apr. 2010.
- [29] E. G. van Putten, A. Lagendijk, and A. P. Mosk, "Optimal concentration of light in turbid materials," *Journal of the Optical Society of America B*, vol. 28, p. 1200, May 2011.
- [30] J. W. Tay, P. Lai, Y. Suzuki, and L. V. Wang, "Ultrasonically encoded wavefront shaping for focusing into random media," *Scientific Reports*, vol. 4, May 2015.
- [31] F. Kong, R. H. Silverman, L. Liu, P. V. Chitnis, K. K. Lee, and Y. C. Chen, "Photoacoustic-guided convergence of light through optically diffusive media," *Optics Letters*, vol. 36, p. 2053, June 2011.
- [32] A. M. Caravaca-Aguirre, D. B. Conkey, J. D. Dove, H. Ju, T. W. Murray, and R. Piestun, "High contrast three-dimensional photoacoustic imaging through scattering media by localized optical fluence enhancement," *Optics Express*, vol. 21, p. 26671, Nov. 2013.
- [33] P. Lai, L. Wang, J. W. Tay, and L. V. Wang, "Photoacoustically guided wavefront shaping for enhanced optical focusing in scattering media," *Nature Photonics*, vol. 9, pp. 126–132, Feb. 2015.
- [34] O. Katz, E. Small, Y. Guan, and Y. Silberberg, "Noninvasive nonlinear focusing and imaging through strongly scattering turbid layers," *Optica*, vol. 1, p. 170, Sept. 2014.

-
- [35] J. Tang, R. N. Germain, and M. Cui, "Superpenetration optical microscopy by iterative multiphoton adaptive compensation technique," *Proceedings of the National Academy of Sciences*, vol. 109, pp. 8434–8439, May 2012.
- [36] R. Fiolka, K. Si, and M. Cui, "Complex wavefront corrections for deep tissue focusing using low coherence backscattered light," *Optics Express*, vol. 20, p. 16532, July 2012.
- [37] J. Jang, J. Lim, H. Yu, H. Choi, J. Ha, J.-H. Park, W.-Y. Oh, W. Jang, S. Lee, and Y. Park, "Complex wavefront shaping for optimal depth-selective focusing in optical coherence tomography," *Optics Express*, vol. 21, p. 2890, Feb. 2013.
- [38] C.-L. Hsieh, Y. Pu, R. Grange, and D. Psaltis, "Digital phase conjugation of second harmonic radiation emitted by nanoparticles in turbid media," *Optics Express*, vol. 18, p. 12283, June 2010.
- [39] I. M. Vellekoop, M. Cui, and C. Yang, "Digital optical phase conjugation of fluorescence in turbid tissue," *Applied Physics Letters*, vol. 101, p. 081108, Aug. 2012.
- [40] X. Xu, H. Liu, and L. V. Wang, "Time-reversed ultrasonically encoded optical focusing into scattering media," *Nature Photonics*, vol. 5, pp. 154–157, Mar. 2011.
- [41] K. Si, R. Fiolka, and M. Cui, "Fluorescence imaging beyond the ballistic regime by ultrasound-pulse-guided digital phase conjugation," *Nature Photonics*, vol. 6, pp. 657–661, Oct. 2012.
- [42] Y. M. Wang, B. Judkewitz, C. A. DiMarzio, and C. Yang, "Deep-tissue focal fluorescence imaging with digitally time-reversed ultrasound-encoded light," *Nature Communications*, vol. 3, Jan. 2012.
- [43] K. Si, R. Fiolka, and M. Cui, "Breaking the spatial resolution barrier via iterative sound-light interaction in deep tissue microscopy," *Scientific Reports*, vol. 2, Dec. 2012.
- [44] Y. Suzuki, J. W. Tay, Q. Yang, and L. V. Wang, "Continuous scanning of a time-reversed ultrasonically encoded optical focus by reflection-mode digital phase conjugation," *Optics Letters*, vol. 39, p. 3441, June 2014.
- [45] H. Ruan, M. Jang, B. Judkewitz, and C. Yang, "Iterative Time-Reversed Ultrasonically Encoded Light Focusing in Backscattering Mode," *Scientific Reports*, vol. 4, May 2015.

-
- [46] B. Judkewitz, Y. M. Wang, R. Horstmeyer, A. Mathy, and C. Yang, “Speckle-scale focusing in the diffusive regime with time reversal of variance-encoded light (TROVE),” *Nature Photonics*, vol. 7, pp. 300–305, Apr. 2013.
- [47] C. Ma, X. Xu, Y. Liu, and L. V. Wang, “Time-reversed adapted-perturbation (TRAP) optical focusing onto dynamic objects inside scattering media,” *Nature Photonics*, vol. 8, pp. 931–936, Dec. 2014.
- [48] E. H. Zhou, H. Ruan, C. Yang, and B. Judkewitz, “Focusing on moving targets through scattering samples,” *Optica*, vol. 1, p. 227, Oct. 2014.
- [49] Z. Huang, “A Review of Progress in Clinical Photodynamic Therapy,” *Technology in Cancer Research & Treatment*, vol. 4, pp. 283–293, June 2005.
- [50] G. C. R. Ellis-Davies, “Caged compounds: photorelease technology for control of cellular chemistry and physiology,” *Nature Methods*, vol. 4, pp. 619–628, Aug. 2007.
- [51] F. Zhang, V. Gradinaru, A. R. Adamantidis, R. Durand, R. D. Airan, L. de Lecea, and K. Deisseroth, “Optogenetic interrogation of neural circuits: technology for probing mammalian brain structures,” *Nature Protocols*, vol. 5, pp. 439–456, Mar. 2010.
- [52] J. W. Lichtman and J.-A. Conchello, “Fluorescence microscopy,” *Nature Methods*, vol. 2, pp. 910–919, Dec. 2005.
- [53] M. A. Thompson, M. D. Lew, and W. Moerner, “Extending Microscopic Resolution with Single-Molecule Imaging and Active Control,” *Annual Review of Biophysics*, vol. 41, pp. 321–342, June 2012.
- [54] M. Polin, K. Ladavac, S.-H. Lee, Y. Roichman, and D. G. Grier, “Optimized holographic optical traps,” *Optics Express*, vol. 13, no. 15, p. 5831, 2005.
- [55] M. A. Taylor, M. Waleed, A. B. Stilgoe, H. Rubinsztein-Dunlop, and W. P. Bowen, “Enhanced optical trapping via structured scattering,” *Nature Photonics*, vol. 9, pp. 669–673, Aug 2015.
- [56] M. A. Taylor, “Optimizing phase to enhance optical trap stiffness,” *Scientific Reports*, vol. 7, Dec. 2017.
- [57] Y. E. Lee, O. D. Miller, M. T. Homer Reid, S. G. Johnson, and N. X. Fang, “Computational inverse design of non-intuitive illumination patterns to maximize optical force or torque,” *Optics Express*, vol. 25, p. 6757, Mar. 2017.
- [58] E. P. Wigner, “Lower Limit for the Energy Derivative of the Scattering Phase Shift,” *Physical Review*, vol. 98, pp. 145–147, Apr. 1955.

- [59] F. T. Smith, “Lifetime Matrix in Collision Theory,” *Physical Review*, vol. 118, pp. 349–356, Apr. 1960.
- [60] P. Ambichl, A. Brandstötter, J. Böhm, M. Kühmayer, U. Kuhl, and S. Rotter, “Focusing inside Disordered Media with the Generalized Wigner-Smith Operator,” *Physical Review Letters*, vol. 119, July 2017.
- [61] S. Rotter, P. Ambichl, and F. Libisch, “Generating Particlelike Scattering States in Wave Transport,” *Physical Review Letters*, vol. 106, Mar. 2011.
- [62] S. Fan and J. M. Kahn, “Principal modes in multimode waveguides,” *Optics Letters*, vol. 30, p. 135, Jan. 2005.
- [63] J. Carpenter, B. J. Eggleton, and J. Schröder, “Observation of Eisenbud–Wigner–Smith states as principal modes in multimode fibre,” *Nature Photonics*, vol. 9, pp. 751–757, Nov. 2015.
- [64] W. Xiong, P. Ambichl, Y. Bromberg, B. Redding, S. Rotter, and H. Cao, “Spatiotemporal Control of Light Transmission through a Multimode Fiber with Strong Mode Coupling,” *Physical Review Letters*, vol. 117, July 2016.
- [65] B. Gérardin, J. Laurent, P. Ambichl, C. Prada, S. Rotter, and A. Aubry, “Particlelike wave packets in complex scattering systems,” *Physical Review B*, vol. 94, July 2016.
- [66] J. Böhm, A. Brandstötter, P. Ambichl, S. Rotter, and U. Kuhl, “*In situ* realization of particlelike scattering states in a microwave cavity,” *Physical Review A*, vol. 97, Feb. 2018.
- [67] M. Kühmayer, “Particlelike states in d-shaped fibers,” Master’s thesis, Vienna University of Technology, 2016.
- [68] M. Bartelmann, B. Feuerbacher, T. Krüger, D. Lüst, A. Rebhan, and A. Wipf, *Theoretische Physik -*. Berlin Heidelberg New York: Springer-Verlag, 2014.
- [69] M. Kühmayer, “Unpublished notes.” 2018.
- [70] D. S. Fisher and P. A. Lee, “Relation between conductivity and transmission matrix,” *Phys. Rev. B*, vol. 23, pp. 6851–6854, Jun 1981.
- [71] H. Egger, J. Gopalakrishnan, and G. Kitzler, “Ngsolve.” <https://ngsolve.org/>.
- [72] J. Schöberl, “NETGEN An advancing front 2d/3d-mesh generator based on abstract rules,” *Computing and Visualization in Science*, vol. 1, pp. 41–52, July 1997.

-
- [73] X. Cheng and A. Z. Genack, “Focusing and energy deposition inside random media,” *Opt. Lett.*, vol. 39, pp. 6324–6327, Nov 2014.
- [74] I. M. Vellekoop and A. P. Mosk, “Universal optimal transmission of light through disordered materials,” *Phys. Rev. Lett.*, vol. 101, p. 120601, Sep 2008.
- [75] M. Horodyski, M. Kühmayer, A. Brandstötter, and S. Rotter, “Manuscript in preparation,”
- [76] J. Schwinger, “On gauge invariance and vacuum polarization,” *Phys. Rev.*, vol. 82, pp. 664–679, Jun 1951.
- [77] V. Lyuboshitz, “On collision duration in the presence of strong overlapping resonance levels,” *Physics Letters B*, vol. 72, no. 1, pp. 41 – 44, 1977.